NASA CONTRACTOR REPORT 177431

Incompressible Viscous Flow Simulations of the NFAC Wind Tunnel

J.M. Champney
Applied & Theoretical Mechanics, Inc.
Oakland, CA. 94605

CONTRACT NAS2-12187
June 1986

NASA

NASA CONTRACTOR REPORT 177431

Incompressible Viscous Flow Simulations of the NFAC Wind Tunnel

J.M. Champney

Prepared for
Ames Research Center
under Contract NAS2-12187
June 1986

National Aeronautics and
Space Administration

Ames Research Center
Moffett Field, California 94035

ABSTRACT

The capabilities of an existing three-dimensional incompressible Navier-Stokes flow solver, INS3D, are extended and improved to solve turbulent flows through the incorporation of zero- and two-equation turbulence models. The two-equation model equations are solved in their high Reynolds number form and utilize wall functions in the treatment of solid wall boundary conditions. The implicit approximate factorization scheme is modified to improve the stability of the two-equation solver. Applications to the three-dimensional viscous flow inside the 80 by 120 feet open return wind tunnel of the National Full Scale Aerodynamics Complex (NFAC) are discussed and described.

TABLE OF CONTENTS

ILLUSTRATIONS

SECTION 1 : INTRODUCTION

Three-dimensional, incompressible turbulent flows are frequently encountered in many industrially important flows, such as low-speed wind tunnels or the space shuttle main engine. These flows represent a class of complex problems of practical importance. The purpose of this work is to offer an engineering tool which can take into account important viscous effects such as separated flow regions, secondary flows, and which can be flexible, accurate and computationally efficient.

To fulfill this goal, an existing computer code, INS3D, developped by Kwak et al. (Ref. 1) for solving the incompressible, Navier-Stokes equations in a three-dimensional, curvilinear coordinate system, is applied. Before describing the applications, the features of the code are briefly outlined.

The INS3D code makes use of the artificial compressibility concept, introduced by Chorin (Ref. 2). It consists in adding a time derivative of the pressure term to the mass conservation equation, and results in solving a system of hyperbolic equations. An implicit time-differencing procedure (Ref. 3) is adopted to march in time until a steady state is reached.

The code has been applied to solve several laminar flows, (Refs. 4, 5 and 6), and turbulence effects have been taken into account by means of a zero-equation model (Ref. 7). In this approach, turbulence is modeled through the use of time averaging procedures which introduce unknown Reynolds stresses into the equations of motion. These stresses are then modeled by relating them to known mean flow quantities.

In the present work, two eddy viscosity models are investigated

1) the Prandtl mixing length zero-equation model (Ref. 8), and 2) the k-epsilon two-equation model (Ref. 9). Eddy viscosity models have been extensivley studied for complex, two-dimensional flows (Refs. 10-12). Their extensions to complex three-dimensional flows are encouraging but deficiencies have been pointed (Ref. 13) in particular, for complex three-dimensional compressible flow fields with large separated zones. The assessment of eddy viscosity models in the INS3D code for complex three-dimensional incompressible flows remains to be done. The goal of this study is to make the INS3D code operational for complex three-dimensional turbulent flows using eddy viscosity models.

In the following sections, the equations of motion, the turbulence models, the numerical methods and wall function boundary conditions used in the simulations are discussed. These are followed by a representative application to the three-dimensional flow inside the 80x120 wind tunnel at NASA-Ames Research Center.

SECTION 2: EQUATIONS OF MOTION

The basic equations used to analyze turbulent flows are the Reynolds-averaged incompressible Navier-Stokes equations. These equations expressed in Cartesian form may be written :

$$\frac{\partial u_i}{\partial x_i} = 0 \tag{1a}$$

$$\frac{\partial u_i}{\partial t} + \frac{\partial u_i u_j}{\partial x_j} = -\frac{\partial p}{\partial x_i} + \frac{\partial \tau_{ij}}{\partial x_j} \tag{1b}$$

According to Refs 2 and 3, equation (1a) is modified as follows:

$$\frac{\partial p}{\partial t} + \beta \frac{\partial u_i}{\partial x_i} = 0 \tag{1a'}$$

where t is time ; x_i are the Cartesian coordinates, u_i are corresponding velocity components, p is the pressure and τ_{ij} is the viscous stress tensor and β is the pseudo compressibility parameter.

The viscous stress tensor includes both molecular and Reynolds-averaged turbulent contributions. By means of the eddy-viscosity hypothesis, the viscous stress tensor is written in the following form:

$$\tau_{ij} = -(\nu + \nu_T)\ (u_{i,j} + u_{j,i}) \tag{2}$$

where ν and ν_T are the molecular and turbulent (eddy) viscosities, and subscript notation has been introduced for partial derivatives.

As mentionned in the introduction, the eddy viscosity for the two-equation models is represented in terms of additional field variables here taken to be s_1 and s_2 so that $\nu_T = \nu_T(s_1,s_2)$. The additional field equations governing s_1 and s_2 are written as

$$\frac{\partial s_i}{\partial t} + \frac{\partial}{\partial x_j}(s_i u_j + q_{ij}) = H_i \qquad (3)$$

$$q_{ij} = -(\nu + \frac{\nu_T}{P_{ri}})\frac{\partial s_i}{\partial x_j} \qquad i = 1,2 \quad j = 1,2,3$$

with $(x_j)_{j=1,2,3} = (x,y,z)$,
where the modeling constants, Pr_1 , Pr_2 are turbulent Prandtl numbers, and H_1 , H_2 are source functions. The source functions depend on s_1, s_2 and $u_{i,j}$, and will be described in detail in the next section.

The equations are written in a dimensionless form with:

$$t = \frac{L\tilde{t}}{U} \qquad x = L\tilde{x} \qquad u_i = U\tilde{u}_i \qquad \nu = UL\tilde{\nu} \qquad (4)$$

$$k = U^2\tilde{k} \qquad \varepsilon = \frac{U^3}{L}\tilde{\varepsilon} \qquad R_e = \frac{UL}{\nu} = \frac{1}{\tilde{\nu}}$$

For applications to curvilinear coordinates (ξ,η,ζ), equations (1) are transformed by means of the following relations:

$$\xi = \xi(x,y,z)$$
$$\eta = \eta(x,y,z) \qquad (5)$$
$$\zeta = \zeta(x,y,z)$$

We will also use the condensed form : $\xi_i = \xi,\eta,\zeta$ for i = 1, 2, or 3. The tildes (~) have been dropped for convenience. The reference length is L, the reference velocity is U.

Further details on this transformation may be found in Ref. 1. The governing equations in conservation-law form are expressed in generalized curvilinear coordinates as :

$$\frac{\partial \hat{Q}}{\partial t} + \frac{\partial}{\partial \xi_i}(\hat{E}_i - \hat{E}_{vi}) = 0 \qquad i = 1,2,3 \qquad (6)$$

where

$$\hat{Q} = \vec{Q}/J = \frac{1}{J}\begin{bmatrix} p \\ u_1 \\ u_2 \\ u_3 \end{bmatrix} \quad ; \quad \hat{E}_i = \frac{1}{J}\begin{bmatrix} u_i \\ u_1 U_i + L_{i1}p \\ u_2 U_i + L_{i2}p \\ u_3 U_i + L_{i3}p \end{bmatrix} \qquad (7)$$

$$\hat{E}_{vi} = \frac{\nu}{J}(\nabla\xi_i . \nabla\xi_j)\frac{\partial}{\partial \xi_j}[0, u_1, u_2, u_3]^T$$

J is the Jacobian of the transformation and

$$U_i = L_{i1}u_1 + L_{i2}u_2 + L_{i3}u_3$$

$$L_{i1} = (\xi_i)_x \; ; \quad L_{i2} = (\xi_i)_y \; ; \quad L_{i3} = (\xi_i)_z$$

are the contravariant velocities and the metrics of the transformation respectively.

Equation (7) is simplified to : $\frac{\nu}{J}(\nabla\xi_i . \nabla\xi_i)\frac{\partial}{\partial \xi_i}(\vec{Q})^T$ (8)

The approximation (8) is valid for nearly orthogonal grids. The use of such approximation results from a compromise in the choice of saving computer time and storage. In the application presented here, the choice of keeping available the maximum number of grid points was made. Therefore, the metrics are not kept in memory and are computed when they are needed and the approximation (8) is made to minimize computing time.

SECTION 3: TURBULENCE MODELS

In this section we will describe the turbulent models used in the present study. As mentioned in the Introduction, these are the zero- and two-equation eddy viscosity models. Advantages and disadvantages of eddy-viscosity models have been studied (Refs. 11 12, 13 and 14), some of these aspects are recalled here.

3.1 Zero-Equation Model

A relatively large number of zero-equation models have been used with the Navier-Stokes equations. These are the simplest of all turbulent models because they require no additional field equation and contain only a few modelling constants. The numerical compatibility of these models is high, which is why they have been widely used. However, zero-equation models are deficient in two important aspects: First, the assumption on the algebraic length-scale that they require is very difficult to specify for complex separated flows, which reduces the generality of the model. Secondly, these models do not account for flow history or stress relaxation effects, which are important in complex flows. However, these models have given reasonable agreement for simple flows, and they are useful for comparison purposes in evaluating and improving performances of more sophisticated models. Here the simplest and the oldest zero-equation model is employed, i.e. the Prandtl mixing length model. This is a two layer model with a modified distance function. An earlier investigation using a modified distance function has been performed by Hung and MacCormack (Ref. 15). The eddy viscosity and related parameters are written below:

$$\nu_T = l^2 \, |\vec{\nabla} \times \vec{u}| \qquad (9)$$

The eddy viscosity is related to the local absolute value of

vorticity, which is invariant with respect to a rotation of the coordinate system, and involves a single unknown parameter: the mixing length l. The specification of this parameter is given below.

The Prandtl mixing length, is given by :

$$l = \min(\kappa\, l_i,\ l_o) \qquad \text{with } \kappa = 0.4 \qquad (10)$$

The inner length or distance function is $l_i = \dfrac{d_\eta\, d_\zeta}{\sqrt{d_\eta^2 + d_\zeta^2}}$,

where d_ζ is the distance from the wall $\zeta = 0$, and d_η is the distance from the two (side and top) walls, corresponding to $\eta=0$.

The definition of the inner length is critical for the evaluation of the turbulence length-scale. This composite formula is designed to account for the size of turbulence eddies or the turbulence mixing length near the corner under the influence of both walls. Note that :

$$\text{If } d_\eta \ll d_\zeta;\ l_i \cong d_\eta$$
$$\text{If } d_\zeta \ll d_\eta;\ l_i \cong d_\zeta$$

The outer length is $l_o = 0.09\ \delta(x)$, where $\delta(x)$ is the boundary layer thickness. A simplified formula for $\delta(x)$ is used in the present study and is obtained from the empirical flat plate formula (Ref. 16):

$$\frac{\delta(x)}{x} = 0.37\ R_{ex}^{-0.2}\ ; \qquad R_{ex} = \frac{Ux}{\nu}$$

x is the streamwise distance from the inflow boundary.
This simplified formula for $\delta(x)$ has been used in the present study because of the great difficulty in computing the boundary layer thickness in the conventional manner by locating the edge

of the boundary layer. Since the main purpose of this work was to implement and make operational the two-equation model in the INS3D code, this simplification was used as a short cut to reach this goal in a short time.

3.2 Two-Equation Model

In these models, two field equations are specified (see Eq. 3). One equation determines the velocity scale, the other the length-scale.

In this work, the high Reynolds number form of the k-ε model is used in conjuntion with wall function boundary conditions. The variable k represents the turbulent kinetic energy, the variable ε is the dissipation rate of kinetic energy. This model is summarized below, further details of this model can be found in Ref. 10.

(k-ε) model: $\quad s_1 = k \quad s_2 = \varepsilon$

$$H_k = P - \varepsilon$$

$$H_\varepsilon = C_1 \frac{\varepsilon}{k} P - C_2 \frac{\varepsilon^2}{k}$$

Making use of the gradient diffusion hypothesis, the term describing the production of turbulence, P, is written as :

$$P = [\nu_T(u_{i,j} + u_{j,i}) - \frac{2}{3} k\delta_{ij}]u_{i,j}$$

The constants in the model are :

$C_\mu = 0.09 \qquad C_1 = 1.45 \qquad C_2 = 1.92$

$P_{rk} = 1.0 \qquad P_{r\varepsilon} = 1.3.$

The choice of these constants are discussed in Reference 17. Briefly, C_μ is determined from the observation that the production and the dissipation in a constant stress layer flow

adjacent to a wall are balanced, convection transport is negligible. The constant C_2 is obtained from grid turbulence results where diffusion and production are zero. Knowing these two constants and the von Karman constant, C_1 can be calculated from the ε equation which is greatly simplified in near wall region. The diffusion constants or Schmidt numbers, P_{rk} and $P_{r\varepsilon}$ were determined from systematic comparisons of computations with experiments for a series of flows.

SECTION 4: NUMERICAL METHODS

The numerical method used to solve the incompressible Navier-Stokes equations is detailed in Ref. 1, it is an implicit, approximately factored finite-difference method due to Beam and Warming (Ref. 18). The same numerical procedure to solve the two-equation turbulence model is employed and is described in Ref. 10.

An important feature of the numerical method not considered in Ref. 10 is the treatment of the turbulence field equations, in particular, the implicit treatement of the turbulence source functions. This treatment follows the work by T.J. Coakley (Ref. 14) and is given here; such a treatment is helpful to the successful numerical implementation of two-equation models. In the present approach, the continuity and momentum equations are solved first and the primitive variables p, u, v, w are updated before going on to solving for the two turbulence variables. Therefore, p, u, v, w are known at the time level n+1 when the resolution of the two-equation model starts. Let us consider the two-equation model system of partial differential equations expressed in curvilinear coordinates:

$$D_t + E_\xi + F_\eta + G_\zeta = S \qquad (13)$$

$D = (k/J, \ \varepsilon/J)$; E, F, G are the turbulent fluxes associated with the directions ξ, η, ζ. This is written as:

$$\frac{\Delta D}{\Delta t} + \frac{\partial E}{\partial \xi}^{n+1} + \frac{\partial F}{\partial \eta}^{n+1} + \frac{\partial G}{\partial \zeta}^{n+1} = S^{n+1}$$

In the INS3D code, continuity and momentum equations are solved first with the pressure and velocity components updated before solving for the turbulent variables k and ε . Therefore, the turbulent source terms are expressed at time n+1 instead of at time n like in the basic algorithm. Then, Taylor expansions

give: $E^{n+1} = E^n + \Delta E = E^n + \frac{\partial E}{\partial D}\Delta D = E^n + A^n \Delta D$

$F^{n+1} = F^n + B^n \Delta D$

$G^{n+1} = G^n + C^n \Delta D$

$S^{n+1} = S^n + K^n \Delta D$

$$A = \frac{\partial E}{\partial D}\ , \quad B = \frac{\partial F}{\partial D}\ , \quad C = \frac{\partial G}{\partial D}\ , \quad K = \frac{\partial S}{\partial D}$$

As a result, a Jacobian Matrix K, derived from a Taylor expansion of the source term appears in the Left Hand Side (LHS) of the finite-difference equations. We write :

$$[1 + \Delta t(\partial_\xi A + \partial_\eta B + \partial_\zeta C - K)]\,\Delta D = \underbrace{-\Delta t\,[\partial_\xi E^n + \partial_\eta F^n + \partial_\zeta G^n - S^n]}_{RHS}$$

The term K is a rather complicated Jacobian matrix which will be approximated by the identity matrix multiplied by a constant. The unfactored algorithm is :

$$[I - \Delta t\ K + \Delta t\ (L_\xi + L_\eta + L_\zeta)]\Delta D = RHS$$

where L_ξ, L_η, L_ζ are three one-dimensional operators. The algorithm is expressed in this convenient form to use the spatial splitting technique, characteristic of the alternating direction-implicit (ADI) scheme. Then, we write

$$(I - \Delta t\ K)\ [I + \Delta t\ (1 - \Delta t\ K)^{-1}\ (L_\xi + L_\eta + L_\zeta)]\ \Delta D = RHS$$

The operators L_ξ, L_η, L_ζ become :

$$L'_\xi = (1 - \Delta t\ K)^{-1}\ L_\xi \qquad \text{etc...}$$

Then, the approximate factorization ADI method is used, and the implicit source term involving the constant becomes product of the time step:

$$[I + \Delta t\ (L'_\xi + L'_\eta + L'_\zeta)]\,\Delta D = \Delta t\ (1 - \Delta t\ K)^{-1}\ RHS$$

is factored as :

$$(1 + \Delta t\, L'_\xi)(1 + \Delta t\, L'_\eta)(1 + \Delta t\, L'_\zeta)\ \Delta D = -\Delta t(1 - \Delta t\, K)^{-1} RHS$$

The choice of K follows the choice of Ref. 14. We set:

$$\Delta\tau = \frac{\Delta t}{1 + \Delta t\, K}$$

A composite formula is used for K :

$$K = \alpha\ (2C_2 \frac{\varepsilon}{k}) + (1 - \alpha)\ 2\frac{(\nu + \nu_T)}{\Delta S^2}$$

$$\frac{1}{\Delta S^2} = \frac{1}{\Delta S_\xi^2} + \frac{1}{\Delta S_\eta^2} + \frac{1}{\Delta S_\zeta^2} \qquad \text{and}$$

$$S_\xi^2 = x_\xi^2 + y_\xi^2 + z_\xi^2$$

$$S_\eta^2 = x_\eta^2 + y_\eta^2 + z_\eta^2$$

$$S_\zeta^2 = x_\zeta^2 + y_\zeta^2 + z_\zeta^2, \qquad x_\xi = \frac{X(J+1) - X(J-1)}{2}\ , \text{ etc ...}$$

For the linear problem, this method is unconditionally stable. This algorithm has not been fully analyzed in the present work. For example, various combinations of the constant α could be tried to determine its optimum value, (i.e. α = 0, 1., 0.5 etc..). In this work, the value of α that performs well is α = 0. The advantage of this algorithm over the case with K = 0, is the enhancement of the stability.

SECTION 5: WALL FUNCTION BOUNDARY CONDITIONS

The use of wall functions was originally advocated by Launder and Spalding (Ref. 19) and applications have recently been extended to complex compressible flows (Ref. 20).

The simplest boundary conditions to solve the Reynolds-averaged Navier-Stokes equations are no slip conditions. However, when turbulence models are used, this simplicity is challenged by the need of special treatment of low-Reynolds number terms, to solve the viscous sublayer. This treatment, called the integration to the wall, varies accordingly to the turbulence model in use (see Ref. 20). The alternative approach, used here, is the use of "wall functions", or the use of the logarithmic law of the wall formula for the velocity profile near the surface. The reasons for this approach are driven by a concern of economy and improved stability of the turbulence model resolution. The use of wall functions eliminates a considerable number of mesh points, and the need to capture the rapid changes in mean flow and turbulence quantities in the near wall region. Another reason of this choice is that the use of wall functions has been demonstrated to perform well for complex flows (Ref. 20), in particular, the predictions of separated flows with the law of the wall are in some cases improved over the same predictions using the integration to the wall approach.

The high Reynolds number form of the two-equation model is employed in conjuntion with the law of the wall procedure, similar to the one developed and tested in the TURF code (Ref. 11) for compressible flows. This formulation is adapted to the INS3D code as follows : the friction velocity u_τ is determined implicitly from the empirical formula (14), given u_2, y_2, ν, E and κ.

$$u_2 = \frac{u_\tau}{\kappa} \ln \frac{E u_\tau y_2}{\nu} ; \qquad E = 9.128 \qquad (14)$$

the subscript 2 denotes the first point from the wall.

The wall shear stress τ_w is obtained from the friction velocity: $\tau_w = u_\tau^2$
We assume : $\tau_{1\frac{1}{2}} \cong \tau_w = (\nu+\nu_{Tw})_{1\frac{1}{2}}(u_2-u_1)/(y_2-y_1)$.
Letting $u_1 = y_1 = 0$ (no slip) enables to compute the effective eddy viscosity at the mid point $1\frac{1}{2}$, which gives $\tau_{1\frac{1}{2}}=\tau_w=(\nu+\nu_T)_{1\frac{1}{2}}u_2/y_2$.

The molecular viscosity ν is sometimes neglected in this formula. The eddy viscosity $\nu_{1\frac{1}{2}}$ mid way between the wall and the first point from the wall is needed to evaluate the viscous fluxes. Two ways were employed :

1. This eddy viscosity is obtained using an average viscosity :

$$\nu_{T1\frac{1}{2}} = \frac{y_2 \tau_w}{u_2} - \nu = \frac{1}{2}(\nu_{T1} + \nu_{T2})$$

2. Another approach is to assume : $\nu_{T1} = 2\left(\frac{y_2\tau_w}{u_2} - \nu\right) - \nu_{T2}$

The first procedure demonstrated to be the best approach, the friction velocity reaches its final value faster.

The eddy viscosity ν_{T2} is computed from the basic formulas for ν_{T2} for each model:

a) zero-equation model: $\nu_{T2} = l^2 \nabla x \vec{u}$

b) two-equation model: $\nu_{T2} = C_\mu \frac{k^2}{\varepsilon}$

In the case of the zero-equation model, one sided differencing in the direction normal to the walls are used to compute the vorticity at the first mesh point off the wall.

In the case of the two-equation model, boundary conditions on the two turbulence variables are needed, these are discussed page 32 of this report.

SECTION 6: RESULTS

The resulting numerical model was applied to the simulation of the flow inside the 80 by 120 feet wind tunnel located at NASA Ames Research Center. A general schematic of the wind tunnel is shown in Figure 1. The design of this wind tunnel is the result of a major effort in aerodynamic design. The theoretical part of this activity was accomplished with the use of singularity-type panel computer code (Refs. 21 and 22). A three-dimensional Euler analysis of this flow has been performed by Kaul et al. (Ref. 23), showing results in good agreement with the experimental data. In the present study, viscous effects are taken into account through the use of turbulence models.

Three computations are reported and compared:

1. A laminar computation with a Reynolds number of 1000.

2. A turbulent computation using the Prandtl mixing length model and the law of the wall boundary condition, at a Reynolds number of 6.6×10^7.

3. A turbulent computation with the two equation Jones Launder model and the law of the wall boundary condition, at a Reynolds number of 6.6×10^7.

6.1 Grid Generation

The computational grid shown in Figures 2 through 8 is the result of intensive efforts performed through trial and error. The three-dimensional grid is a combination of algebraic procedures and available elliptic and parabolic grid generation computer programs. Figure 2 represents the ground plane, the

inlet part was generated by the parabolic grid generation program of T.A. Edwards (Ref. 24). The nozzle part was generated by an elliptic grid generation program (Kristin Hessenius'private communication). Figure 3 is an enlargement of the inlet region in the ground plane, with the K-lines emerging perpendicularly from the side wall (K = 1). This two-dimensional grid is rotated around the K=KMAX axis to discretize the full computational domain. Figure 4 shows the grid in the vertical plane (L = LMAX-1). Figure 4 a is an enlargement of the inlet lip area, generated by the parabolic grid generation program (Ref. 24). Figure 5 is the cross section grid downstream in the rectangular test section. Figures 6 a and b represent two perspective views of the three-dimensional grid, (a) viewed from the wind tunnel entrance and (b) viewed from the exit. The vertical plane, L = LMAX-1, is a plane of symmetry. The advantages of this grid are :

1. It can be mapped into a cube.
2. Points can be clustered only close to rigid boundaries.
3. A zonal approach is not necessary. This grid results in a one block grid and avoids the complications of patching grids.
4. Orthogonality of the grid lines is accomplished at the rigid boundaries.

A disadvantage is that the line K = KMAX is a singularity line where all the L-lines are merging together (at the bottom wall in the symmetry plane). This singularity caused some difficulties in applying numerical boundary conditions, and this will be reported later.

This grid was used for the laminar computation. It employs 93 planes in the streamwise direction (JMAX = 93), 45 planes in the spanwise direction (KMAX = 45), and 25 rotated planes (LMAX = 25).

For the turbulent computations, the grid points had to be redistributed to satisfy the criterion of validity of the law-of-the wall. When applying the law of the wall boundary conditions, special attention must be given to the first spacing from the wall, since the law of the wall is valid for :

$$20 < y^+ < 1000 \qquad \text{approximately}$$

where $y^+ = \frac{u_\tau d}{\nu} = \frac{u_\tau R_{ex} d}{Ux}$; $R_{ex} = \frac{Ux}{\nu}$

d is the distance from the wall of the first mesh point, x is the streamwise distance from the grid line J = 1.
For a turbulent flow above a flat plate: $\frac{u_\tau}{U} = \sqrt{\frac{\tau_w}{U^2}} = \sqrt{.0296 R_{ex}^{-1/5}}$ (Ref. 16)
Therefore, the spacing of the first mesh point is defined by the algebraic formula :

$$d = 5.8 \times R_{ex}^{-.9} y^+$$

After trial and error, the first spacing of the final "turbulent" grid is obtained with an initial y^+ of 600, resulting in a first spacing from the wall test section of 0.001 approximately. The K and L grid lines were redistributed as shown in Figures 7 and 8, the final grid size is :

JMAX = 83, KMAX = 33, LMAX = 33.

6.2 Laminar solution

The goal of the present study is to perform turbulent simulations of the 80 by 120 feet wind tunnel, however, it is necessary to begin with a laminar simulation that will help defining initial flow conditions, boundary conditions, time steps and that will be used as a comparison with the turbulent computations.
The Reynolds number is 1000 and is based on half the width of the wind tunnel (equal to 60 feet).

Initial conditions.

The dimensionless pressure is set to 1 everywhere in the flow field. The initial values of the velocity are scaled to conserve the mass flux rate at the outflow.

Boundary conditions.

At the walls: zero-gradient extrapolation for the pressure and no-slip condition for the velocity.

At (singularity point) K=KMAX: no slip boundary conditions for velocity components and pressure were employed at first. Then , from comparisons of computations with experiments, it appears that two point extrapolations of the velocity components were the most appropriate boundary conditions.

At the inflow boundary: the inflow boundary is placed sufficiently far upstream so that the velocity gradients are small here. The stagnation pressure and flow direction (taken parallel to the grid line directions) are prescribed.

At the outflow: a simple one point extrapolation is used for the velocity components and pressure. This is the most stable boundary condition. However, because this boundary condition does not automatically conserve the mass, at the start of the computation mass weighting procedures on the pressure and velocity, as described in Ref. 4 are employed.

The results of this computation are shown in Figures 9 through 16. The velocity vector plots in the streamwise direction are shown in Figure 9 for the plane L=16 (which runs diagonally accross the test section). A separation bubble immediatly downstream of the cowl, was observed experimentally but is not predicted by the

computation. This is probably attributed to a too coarse grid spacing. The choice of a coarse spacing in the inlet area was made so that sufficient grid points could be used in the area of the test section. Figure 10 shows the crossflow velocity vectors at x = 210 ft, at the beginning of the test section. Figure 11 shows the crossflow velocity vectors at x= 240 ft.

Figure 12 shows the variation of the axial velocity (normalized by the test-section velocity) with the spanwise coordinate, y, at an x station situated 27 ft upstream of the inlet, close to the z = 0 plane. Indicated on this Figure are the results of the inviscid analysis (Ref. 23), referred to as "inviscid" on this Figure and the following ones. Experimental measurements are indicated by circles. We observe that the inviscid analysis seems to agree better than our viscous analysis, however, this location x = -27 feet, has the coarsest grid spacing, coarser than the inviscid analysis. Also, the viscous results are obtained by three-dimensional interpolation which introduces an absolute error of about 5%. Figure 13 shows a variation of the normalized axial velocity with the vertical coordinate z at x = -27 ft, near the symmetry plane between the two side walls of the tunnel. Figure 13 shows the INS3D results in disagreement with the experimental data and the inviscid solution, at the time of this computation, this was attributed to the use of a constant eddy viscosity model (laminar) that is known to overpredict the thickness of boundary layers. However, the same discrepancy was observed with the turbulent solutions, action to correct it was taken at that time and this will be described in the next subsection. We will see that this is caused by the use of no-slip condition at K=KMAX, and the use of two point extrapolation formula for the velocity components resulted in improved agreement of the computation with the experimental measurements.

Figure 14 shows resultant velocity along the center line (y=z=0)

versus downstream distance from the cowl to the test section. The results are compared with the panel method and with the inviscid method (Ref. 23). The inviscid theory results are for the velocity at the ground. The laminar results are for the velocity mid way between the ground plane and the top plane, so that they can be compared with inviscid theories. In this case, the laminar velocity variation agrees with the panel method results better than with the U. Kaul's results Figure 14 also shows similar comparisons for the tunnel floor pressure distribution versus the downstream distance from the cowl to the test section. We observe some discrepancy in the inlet cowl area. Downstream the inviscid and laminar results are in better agreement.

Figure 15 presents the pressure variation with the downstream distance on the side wall centerline near the z = 0 plane. The comparison between the computations and the experiments is good except near the separation bubble where the pressures given by the laminar simulations are underpredicted with respect to the experiments and inviscid solutions.

Discussion: Figure 11 has shown the existence of weak longitudinal vortices in the test section, one close to the floor center-line, the other close to the top surface. The origin of this vorticity in the flow was not clear and a concern was that this vorticity could be created at the inflow by a poor inflow boundary condition. Figure 16 shows how they originate by presenting velocity vectors in the boundary layer at L=3, L=5 and at the edge of the boundary layer and it is concluded that these vortices result from viscous effects. Because of the side wall contraction, a negative pressure gradient is created crosswise, this deflects the fluid toward the center, the slow moving fluid of the boundary layer is deflected faster than the fluid in the main "inviscid" flow. Downstream of the contraction, the streamline curvature changes and the situation is reversed.

Figure 16 a shows the downstream velocity vectors in the boundary layer directed toward the side wall, Figure 16 c shows the downstream velocity vectors outside the boundary layer directed toward the center line, this effect causes the flow to rotate. These vortices have been studied experimentally (Refs. 25-27), they will occur in laminar boundary layers as well as turbulent. Other than that, the tendency of the flow to be directed toward the center of the plane is observed, as this was also seen in flow-visualization studies.

6.3 Zero-equation model solution

The results obtained with the zero-equation model solution are shown in Figures 17 through 27.

The zero-equation model computations were initialised from the same solution than the one employed for the laminar computation. The boundary conditions were at first unchanged from the laminar solution.

Figures 17 through 21 present quantitative results compared with inviscid theories and experiments. Figures 22 through 27 present qualitative results as vector plots.

Figure 17 presents the normalised axial velocity variation with the spanwise distance at x = -27 feet. We observe good agreement with the experimental data, close to the wall and in the center of the wind tunnel (y=0). Mid way the INS3D results overpredict the axial velocity variation, however, it should be recalled that the grid spacing is particularly coarse in this region and this could explain this apparent discrepancy.

Figure 18 presents the normalized axial velocity variation with height z at x = -27 feet. The dotted line indicates the results

obtained when a no-slip boundary condition was used at K=KMAX, resulting in a disagreement with the inviscid solution and experiments. At first, it was believed that the inflow boundary condition was the cause of this problem, but various inflow velocity profiles were tried (with a boundary layer and without a boundary layer), resulting in the same results. Then, the boundary condition at K=KMAX was modified instead of using no-slip condition, zero-gradient in the z-direction (actually K direction) was employed, i.e. all quantities at K=KMAX for all L planes are set equal to the corresponding value at K=KMAX-1 and L=LMAX-1. This provided improved agreement, the INS3D results are the solid line in Figure 18. From now on, all the results presented were obtained with this boundary condition.

Figure 19 presents the resultant velocity variation with the downstream distance, the INS3D velocity results are evaluated in the center of the wind tunnel on the axis of symmetry so that they can be compared with the inviscid theories. Figure 20 shows the tunnel floor centerline pressure variation with the downstream distance. Indicated in Figures 19 and 20 are the results of the inviscid analysis (Ref. 23) and of the panel method. We observe some discrepancy of the pressure variation in the inlet lip area, while the three computed results agree downstream of the inlet tunnel.

Figure 21 shows the pressure variation on the side wall centerline with the downstream distance compared with the inviscid analysis and experiments. Here too, we observe some discrepancy of the pressure variation in the inlet lip area and this is attributed to the deficiency of the computation in not predicting the separated flow in this area. We think that this is caused by a too coarse mesh and the zero-equation model itself.

Figures 22 and 23 present results of velocity vector plots in the plane L=22 and L=15. Figure 24 is an enlargement of the velocity vector plot in the plane L=15 near the inlet cowl, we observe that the velocity profiles in the most curved part of the inlet cowl seem to be near separation.

Figures 25 a, b, c show crossflow velocity vector plots at three locations, x=32 feet, x= 164 ft, x= 228 ft. Figures 25 a and b show the flow converging toward a point on the symmetry plane. Figure 25 c indicates the existence of a weak vortex in the middle of the test section. As a comparison, we chose to show Figure 26: crossflow velocity vectors at the same location than the one of Figure 25 c. The results of Figure 26 were obtained with the no-slip boundary condition for the velocity at K=KMAX and we observe that the qualitative features of the flow are quite different from the one observed on figure 25 c. The computation using no-slip boundary condition for the velocity at K = KMAX predicts two vortices, one close to the floor, the other close to the top, while the computation using zero-gradient extrapolation for the velocity indicates the presence of a single vortex, in the center of the computational domain.

Figure 27 shows the velocity profile along the line K=22, in the center of the test section.

6.4 Two-equation model solution

Figures 28 to 38 shows the results obtained with the two-equation model.

The same computational grid as the one used for the zero-equation model solution was utilized. The two-equation model solution was restarted from the zero-equation model solution, with free stream values of k and ε used for initial conditions.

Free stream values. An important aspect of the k and solution is the determination of the free stream values, and this is discussed here. Free stream values of the two turbulent variables appear to control the stability of the solution. If the free stream values are too large, the turbulence kinetic energy and the turbulence dissipation cannot diffuse, the eddy viscosity remains null and the solution is laminar. If these values are too small, and in particular, the value of the turbulence dissipation, the eddy viscosity becomes unrealistically large, causing the computation to become unstable. These values were determined by trials and errors and finally, the ratio of eddy viscosity to laminar viscosity was set equal to 0.1, with $k = \sqrt{10} \times 10^{-7}$, ε is deduced from these two values and from the Kolmogorov formula.

Boundary conditions.

The boundary conditions on the pressure and velocity components were unchanged from the one used for the zero-equation model solution. Associated with the use of wall functions, boundary conditions on the two turbulence variables are needed. Two alternative wall boundary conditions on k and ε were tested:

1. $k_w = \dfrac{u_\tau^2}{\sqrt{C_\mu}}$ with $k_2 = k_w$ and $\varepsilon_2 = \dfrac{u_\tau^3}{\kappa y_2}$, y is the distance from the wall (15)

2. $k_3 = k_2 = k_w$ (extrapolation from interior), and $\varepsilon_2 = \varepsilon_3 y_3 / y_2 = \varepsilon_w$, 3 indicates the 2nd mesh point from the wall. (16)

These boundary conditions are critical in getting a good start of the computations. Attempts to start computations with the boundary conditions (16) failed. At the start of a computation, the friction velocity is small, the k and ε values are small also, and with the boundary conditions (15), k and ε profiles develop smoothly. however, it was observed that the friction

velocity obtained from the law of the wall does not grow as fast as the k and ε values do. As a result, a small discontinuity in the profiles of k and ε was observed and although the computation remains stable, the accuracy of the k and ε quantities near the wall was in question. At that point, a switch to boundary conditions (16) was made to insure a smooth monotonic growth of the k and ε profiles, and the friction velocity is allowed to adjust to its steady flow value. After about 1000 cycles, the solution is close to convergence, and boundary conditions (15) and (16) provide similar results.

While performing these computations, a serious stability problem was encountered and is disccused here. It was found that, once the k and ε profiles have developed, the solution could not remain stable. The problem is caused by ε reaching its free stream value too quickly at the fifth mesh point from the wall, while the k profile retains a monotonically decreasing behaviour. This results in an eddy viscosity too large. Many attempts to stabilize the solution failed. These attempts consisted in trying various combinations of the boundary conditions on k, ε and on the eddy viscosity, and in using a small time step. At that point, the stability of the k-ε solution algorithm was in question, and the following test was performed. The two-equation model solution was restarted with the converged zero-equation model solution. The eddy viscosity solution given by the zero-equation model was "frozen" while all the other variables, pressure, velocity and turbulence variables were computed. It was observed that the k and ε profiles develop smoothly, the computation remains stable, and a relatively large time step could be used. From this test, we deduced that the k and ε algorithm was numerically compatible and that our problem was an inaccuracy on the calculation of ε caused by a too coarse mesh. A test was introduced in the computation : if ε is less or equal to its freestream value and k is greater than its freestream

value, ε was set equal to : $$\varepsilon_K = \frac{\varepsilon_{K-1} y_{K-1}}{y_K}$$

This formula is based on the experimental measurements of Klebanoff for flat plates (Ref. 28). This was sufficient to provide ε with a smooth transition from its computed value to a fixed freestream value. The effect was rather spectacular and stabilized the computation. However, this is only a temporary fix and given a finer grid spacing, this condition would probably become unnecessary.

Figures 28 through 32 are a set of quantitative results for the two-equation model, similar to the ones shown for the zero-equation model. We observe that the two-equation model solution provides agreement with inviscid theories and experiments similar to the results obtained with the zero-equation model. In particular, in Figure 32, we observe that in the inlet cowl area the pressure variation is underpredicted by the two-equation model and exhibit a relatively strong variation. To improve agreement in this area, we believe a finer grid spacing would be helpful.

Figures 33 through 38 show velocity vector plots illustrating the qualitative features of the flow field. Velocity vectors in the plane L = 22 are shown in Figure 33. Figure 34 presents an enlargement of the velocity vector plot in the plane L=22 near the inlet cowl, the predicted boundary layer thickness is thin, no separation is observed and this agrees with experimental observation. Velocity vectors in the plane L = 15 are shown in Figure 35. Figure 36 is an enlargement of the velocity vector plot in the plane L=15 near the inlet cowl where separation was observed experimentally. Here, we observe a stronger gradient variation in the boundary layer in spite of the coarse mesh

(velocity vectors for all grid points are plotted), the velocity profile in the cowl center appears to be close to separation. Given a finer spacing, separation might be predicted, as observed in experiment.

Figures 37 a and b show velocity vector plots in the cross-section of the wind tunnel at x = 32 feet and x = 228 feet. At x = 228 feet, we observe a weak vortex in the middle of the test section, caused by the lateral divergence of the streamlines which intensifies the lateral component of vorticity.

Figure 38 compares eddy viscosities and velocity profiles obtained with the zero- and two-equation model at x= 210 feet along the diagonal line L=22. We note here that the boundary-layer thickness predicted by the two-equation model was somewhat larger than the one given by the zero-equation model. With only 10 grid points in the boundary layer, the coarse mesh inhibits an accurate prediction of the boundary layer thickness. For instance, at x = 210 feet along the line L = 22, the boundary layer thickness is such

$$7.2 \text{ feet} < \delta < 9.6 \text{ feet} \quad \text{(zero-equation model)}$$

$$9.6 \text{ feet} < \delta < 12 \text{ feet} \quad \text{(two-equation model)}$$

Figure 39 shows the turbulence kinetic energy and turbulence dissipation curves at x = 210 feet, along the line L=22. In this Figure, a rapid decrease in the dissipation toward the outer edge of the boundary layer is observed, this sharp decrease occurs within three mesh points from the wall, causing the eddy viscosity to become large. Experimental observation (Ref. 28) confirms this behaviour.

SECTION 7: COMPUTER EXECUTION TIME

The computations reported here require approximately:

a) laminar case: 0.0001 seconds per grid point per iteration,
b) zero-equation model case: 0.00011 seconds per grid point per iteration,
c) two-equation model case: 0.00014 seconds per grid point per iteration.

Typically, 700-1200 iterations are required for laminar solutions, and about 1500 iterations are required for turbulent solutions. However, the two-equation model solutions reported here, were run up to 3000 iterations to gain confidence in the stability of the computation but 1000 to 1500 iterations appear sufficient to reach a converged solution. In the two-equation model solution, the residuals of the two turbulence variables decrease quickly (within 500 cycles) by three order of magnitude and then decrease slowly by an approximate factor of 0.0002 per cycle.

For the original algorithm, the largest time step that maintains the stability of the code was 0.003. The time step used to start computations was 0.0001, and was increased progressively to 0.003 up to 700 cycles. The zero-equation model and the two-equation model solution employs the same time step. The laminar solution was obtained with a coarser grid and the largest time step was 0.007. The algorithm modification described in Section 4 was not fully investigated because of lack of time, however, it was observed to perform best after about 500 cycles, (the time step could be increased faster). At the start of a computation no significant improvement on the size of the time step was noted. We feel that this algorithm modification is promising and more in-depth investigation needs to be done.

SECTION 7: CONCLUDING REMARKS

This section summarizes our conclusions, the first subsection outlines the accomplishements of this effort, the second subsection attempts to state objectively the deficiencies of this numerical simulation and gives recommendations for future improvements of viscous three-dimensional simulations.

7.1 Accomplishements.

1. Zero- and two-equation turbulence models have been incorporated into the INS3D code, including special boundary conditions appropriate to the use of wall functions. This procedure enables the use of coarser mesh spacing near the wall, compared with integration to the wall procedures (where no slip boundary conditions are used) and leads to greater stability and efficiency.

2. Laminar and turbulent solutions (with a zero-equation model and with a two-equation model) were computed and the results were compared with available experimental measurements and with inviscid solutions.

3. These computations simulate a flow in which viscous effects, as measured by extent of separation, were small so that the results obtained using the INS3D code should be (roughly) comparable to the results obtained using inviscid codes. This is what was observed. Relatively minor differences from inviscid results were noted for the pressures and axial velocities.

4. The modifications to improve the stability of the algorithm was introduced , but not extensively tested.

For the present, the results are inconclusive regarding improvements in convergence rate.

5. A new simple-single block three-dimensional grid was developed. However, some improvements could be made, in particular, by increasing the number of mesh points.

7.2 Recommendations.

1. The numerical algorithm modification for improving the stability of the computations was not optimized, and more work (following the outlines given in Section 4) is required to make this modification fully efficient.

2. The solutions in the inlet region do not predict the separation observed in experiments, this is probably due to a lack of resolution. A finer grid could cure this problem, or a new type of grid might be required. The best possible grid is an orthogonal single block grid and a three-dimensional elliptic grid generator code would be very helpful.

3. The grid singularity at K=KMAX caused some difficulties regarding the use of boundary conditions. Although changing from no slip to zero-gradient type of boundary conditions imroved the solutions, more improvement is needed, because of the retardation of velocity profiles as the singularity is approached. This could also be possibly caused by the mesh discontinuity along the diagonal or by the use of the thin layer Navier-Stokes equations rather than the full Navier-Stokes equations. We think that it is essential to use the full Navier-Stokes equations in the predictions of three-dimensional

viscous flows, associated with a more regular grid.

4. The two-equation model solutions are not entirely satisfactory, a special stabilizing fix was needed to achieve stable solutions. Here too, more work is needed on wall funtion boundary conditions to remove this problem.

We established the importance of using different models (constant eddy viscosity (laminar), zero-equation and two-equation models) combined with experimental comparisons. Such a process is essential to provide reliable predictions, in Computational Fluid Dynamics.

REFERENCES

1. Kwak, D., Chang, J.L.C., Shanks, S.P. and Chakravarthy, S.R., "An incompressible Navier-Stokes Flow Solver in Three-Dimensional Curvilinear Coordinate System Using Primitive Variables," AIAA Paper 84-0253, AIAA 22nd Aerospace Sciences Meeting Reno, Nevada, January 1984.

2. Chorin, A.J., "A Numerical Method for Solving Incompressible Viscous Flow Problems," Journal of Computational Physics, Vol. 2, 1967, pp. 12-26.

3. Steger, J.L. and Kutler, P., "Implicit Finite-Difference Algorithm for Hyperbolic Systems in Conservation-Law Form," Journal of Computational Physics, Vol. 22, Sept. 1976, pp. 87-110.

4. Chang, J.C.L., Kwak, D., and Dao, S.C., "A Three-Dimensional Incompressible Flow Simulation Method and its Application to the Space Shuttle Main Engine, Part 1: Laminar Flow,: AIAA Paper 85-0175, Reno, Nev., 1985.

5. Kaul, U.K., Kwak, D. and Wagner, C., " A Computation Study of Saddle Point Separation and Horshoe Vortex System," AIAA Paper 85-0182, AIAA 23rd Aerospace Sciences Meeting, Reno, Nevada, January 1985.

6. Rogers, S.E., Kwak, D. and Kaul, U.K., "On the Accuracy of the Pseudo-compressibility Method in Solving the Incompressible Navier-Stokes Equations," AIAA Paper 85-1689, Cincinatti , Ohio, July 1985.

7. Chang, J.L.C., Kwak, D., Dao, S.C. and Rosen, R., "A Three-dimensional Incompressible Flow Simulation Method and its Application to the Space Shuttle Main Engine, Part II - Turbulent Flow," AIAA Paper 85-1670, Cincinatti, Ohio, July 1985.

8. Prandtl, L., "The Mechanics of Viscous Fluids," in Aerodynamic Theory, Vol. III, Durand, W.F. (Ed.), Pasadena, California, 1943.

9. Jones, W.P. and Launder, B.E., "The Predictions of Laminarization with a Two-Equation Model of Turbulence," international Journal of Heat and Mass Transfer, Vol. 15, 1972, pp. 303-314.

10. Kaul, U.K. and Kwak, D., "Computations of Internal Turbulent Flow with Large Separated Flow Regions," AIAA Paper 85-1687, Cincinatti, Ohio, July 1985.

11. Coakley, T.J., "A Compressible Navier-Stokes Code for Turbulent Flow Modeling," presented at the University of Tennessee, March 1984.

12. Viegas, J.R. and Horstman, C.C., "Comparison of Multiequation Turbulence Models for Several Shock Separated Boundary Layer Interaction Flows," AIAA Paper 78-1165, Seattle, Washington, 1978.

13. Horstman, C.C., Kussoy, M.I., and Lockman, W.K., "Computation of Three-dimensional Shock-Wave/Turbulent Boundary-Layer Interaction Flows," Presented at Third Symposium on Numerical and Physical Aspects of Aerodynamics Flows, Long Beach, CA., Jan. 1985.

14. Coakley, T.J., "Turbulence Modeling Methods for the Compressible Navier-Stokes Equations," AIAA Paper 83-1958, Jul. 1983.

15. Hung, C.M. and MacCormack, R.W., "Numerical Solution of Three-dimensional Shock Wave and Boundary Layer Interaction," AIAA Journal Vol. 16, pp. 1090-1096.

16. Schlichting, H., "Boundary-Layer Theory," MacGraw-Hill Book Company, Seventh Edition 1978.

17. Jones, W.P., and Launder, B.E., "The Prediction of Laminarization and its Application to Thin Shear Flows," Journal of Fluid Mechanics, Vol. 52, 1972, pp. 609-638.

18. Beam, R.M. and Warming, R.F., "An Implicit Finite-Difference Algorithm for Hyperbolic Systems in Conservation-Law Form," Journal of Computational Physics, Vol. 22, Sept. 1976, pp. 87-110.

19. Launder, B.E. and Spalding, D.B., Mathematical Models of Turbulence, Academic Press, 1972.

20. Viegas, J.R. and Rubesin M.W., "Wall-Function Boundary Conditions in the Solution of the Navier-Stokes Equations for Complex Compressible Flows," AIAA Paper 83-1994, Danvers, Massachussetts, 1983.

21. Maskew, B., "Program VSAERO: A Computer Program for Calculating the Non-Linear Aerodynamic Characteristics of Arbitrary Configurations," NASA CR-166476, Dec. 1982.

22. Ross, J.C., Olson, L.E., and Meyn, L.A., "A New Design Concept for Indraft Wind-Tunnel Inlets with Application to the National Full-Scale Aerodynamics Complex," AIAA Paper 86-0043, AIAA 24th Aerospace Sciences Meeting, Jan. 1986, Reno, Nevada.

23. Kaul, U.K., Ross, J.C. and Jacoks, J.L., "A Numerical Simulation of the NFAC (National Full-Scale Aerodynamics Complex) open-Return Wind Tunnel Inlet Flow," AIAA Paper 85-0437, AIAA 23rd Aerospace Sciences Meeting, Reno, Nevada, January 1985.

24. Edwards, T.A., "Noniterative Three-Dimensional Grid Generation using Parabolic Partial Differential Equations," AIAA 23rd Aerospace Sciences Meeting, Reno, Nevada, AIAA Papaer 85-0485, January 1985.

25. Mokhtari, S. and Brashaw, P., "Longitudinal Vortices in Wind Tunnel Wall Boundary Layers," Aeronautical Journal, June/July 1983, pp. 233-236.

26. Bansod, P. and Bradshaw, P., "The Flow in S-shaped Ducts,", Aeronautical Quarterly, May 1972, Vol. 23, pp. 131-140.

27. Cebeci, T. and Bradshaw, P., "Momentum Transfer in Boundary Layers," McGraw-Hill Book Company, Hemisphere Publishing Corporation, pp. 321-323.

28. Hinze, J.O., "Turbulence," Second Edition , 1975, McGraw-Hill Book Company, series in Mechanical Engineering, p. 647.

SPEED RANGE: 0.15
(Mach No.) (168 ft/sec)

TEMP. RANGE: Ambient

REYNOLDS NO: 0 - 1.1
(Per ftx10^{-6})

DYNAMIC PRES: 0 - 34
(lb/ft^2)

STAGNATION PRES:
(psia) Atmospheric

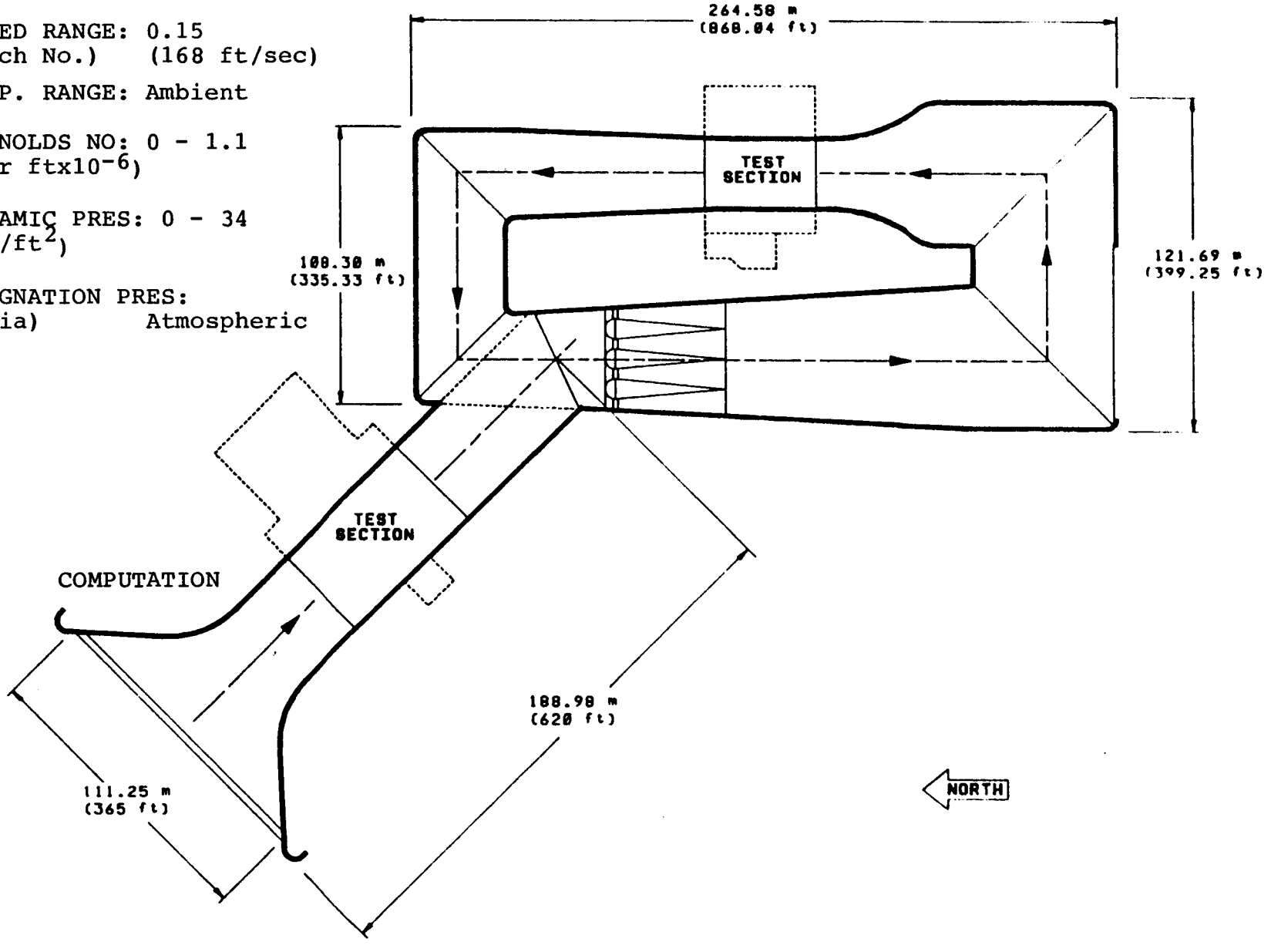

Figure 1. Schematic of the 80x120 ft Wind Tunnel.

Figure 2. Planar grid in the z-plane, L =1.

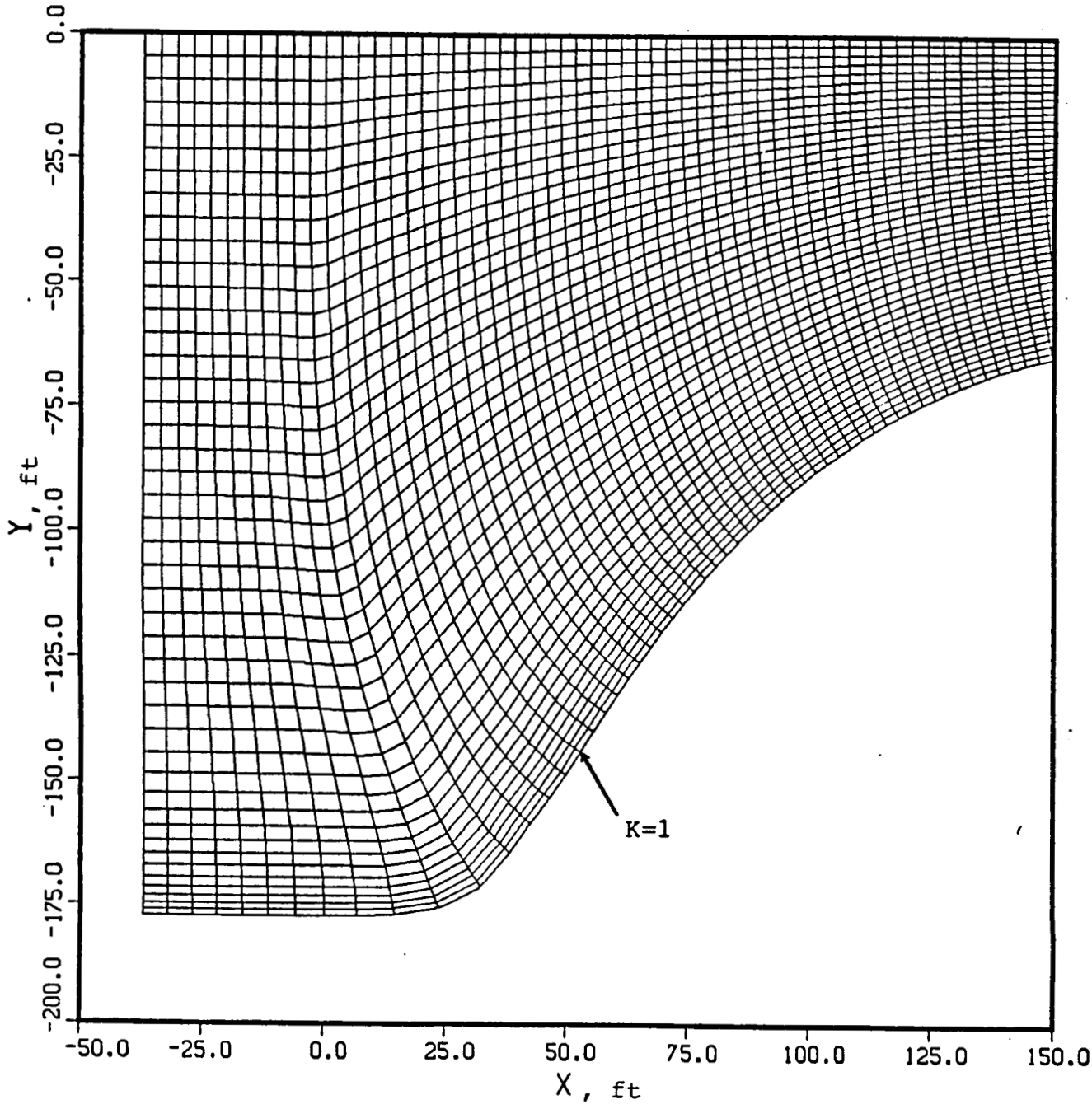

Figure 3. Grid enlarged near the inlet cowl.

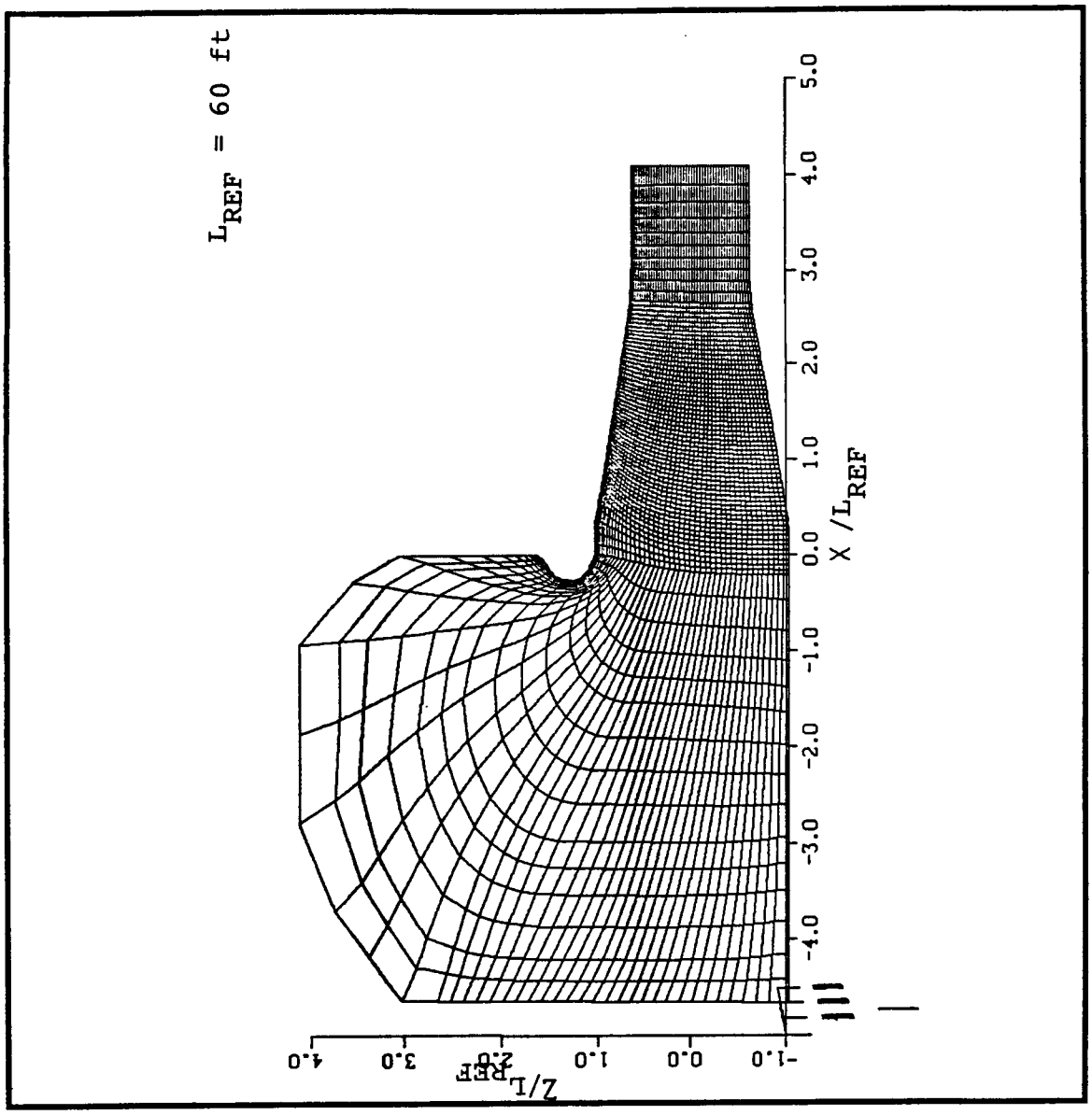

Figure 4. Planar grid in the y-plane, y = 0.

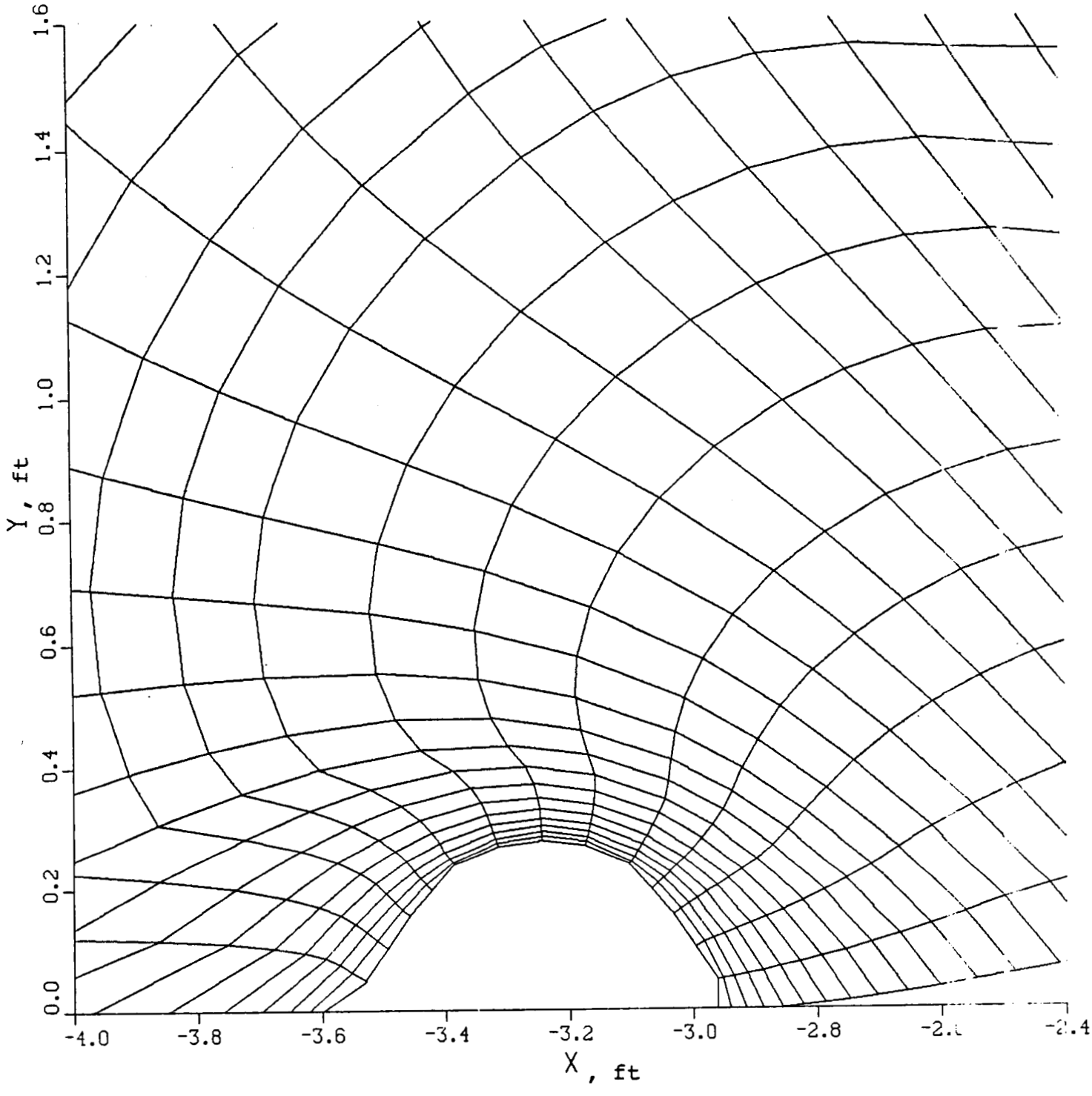

Figure 4 a. Grid enlarged near the inlet lip.

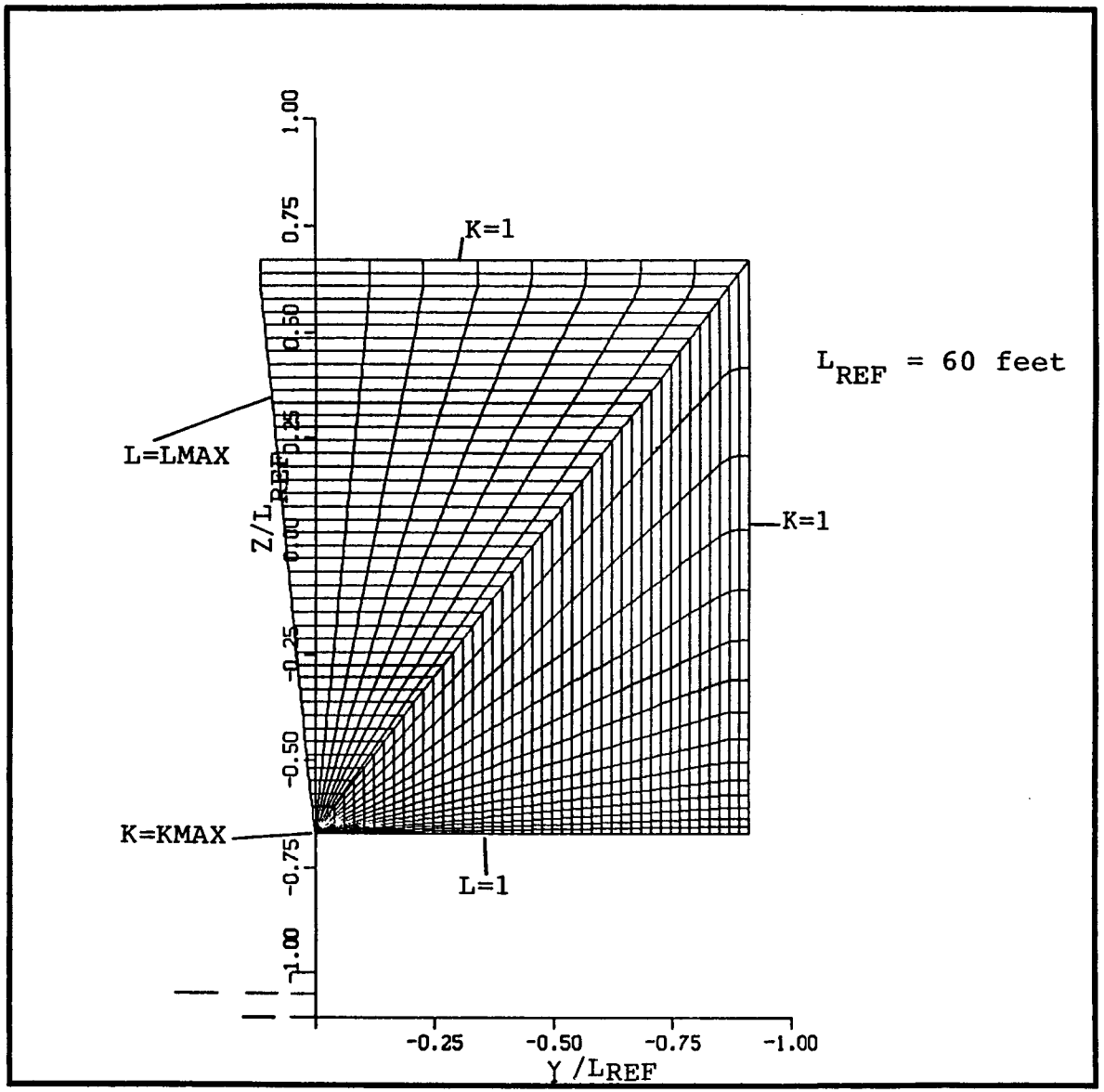

Figure 5. Cross-section plane grid, x = 210 feet.

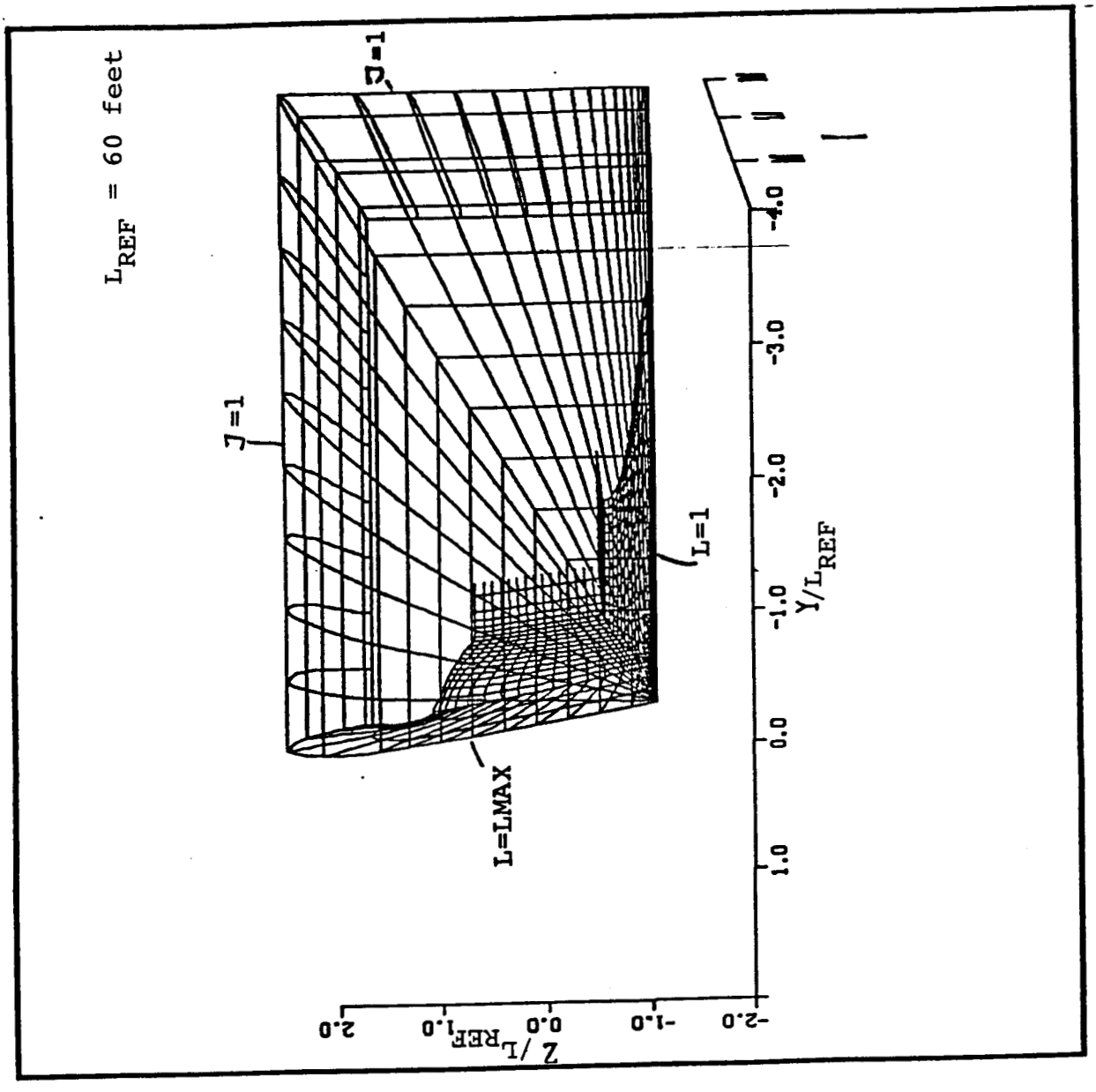

Figure 6 a. Grid plot showing the surfaces J=1, L=1, L=LMAX.

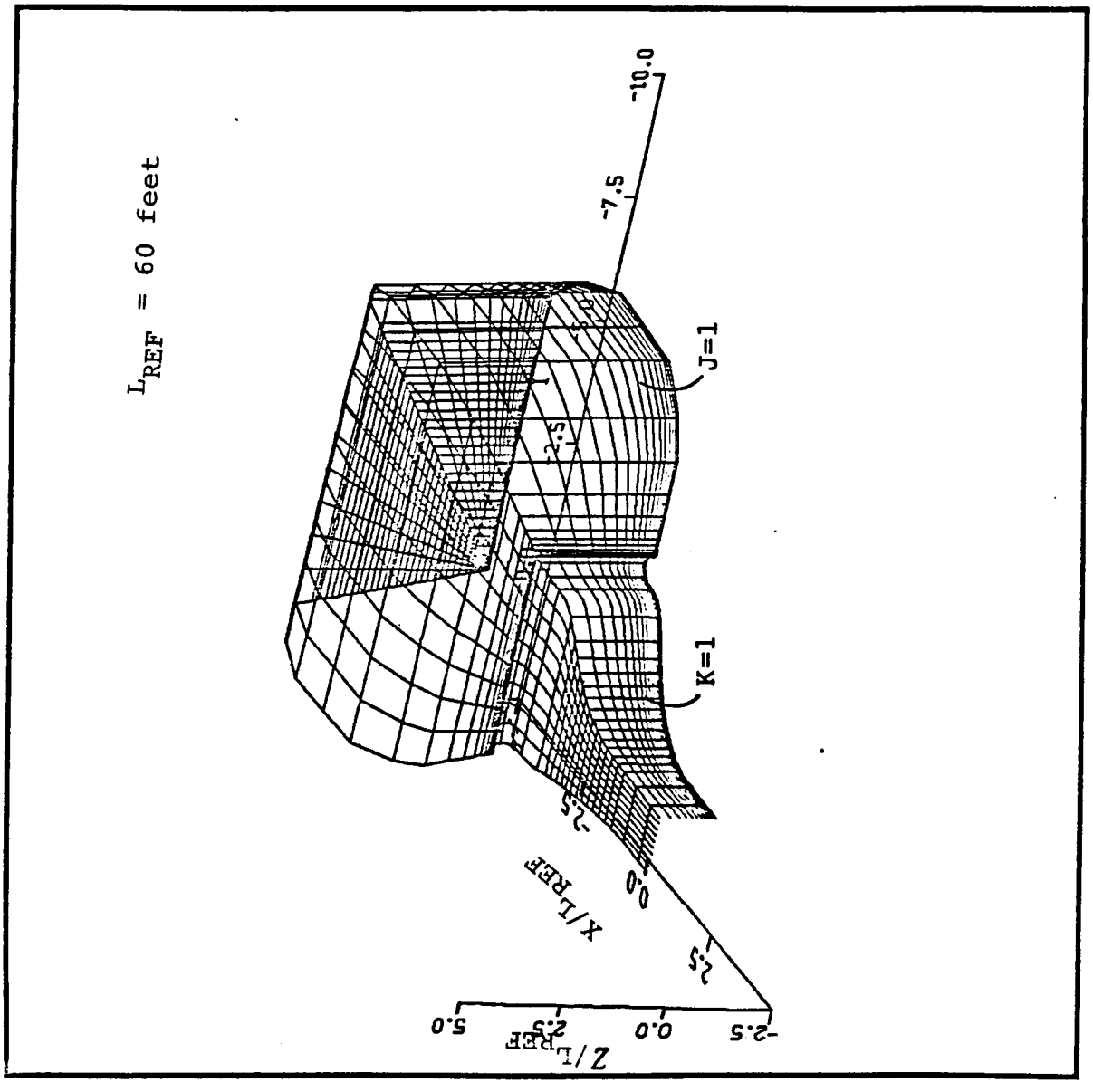

Figure 6 b. Grid plot showing the surfaces J=1, K=1.

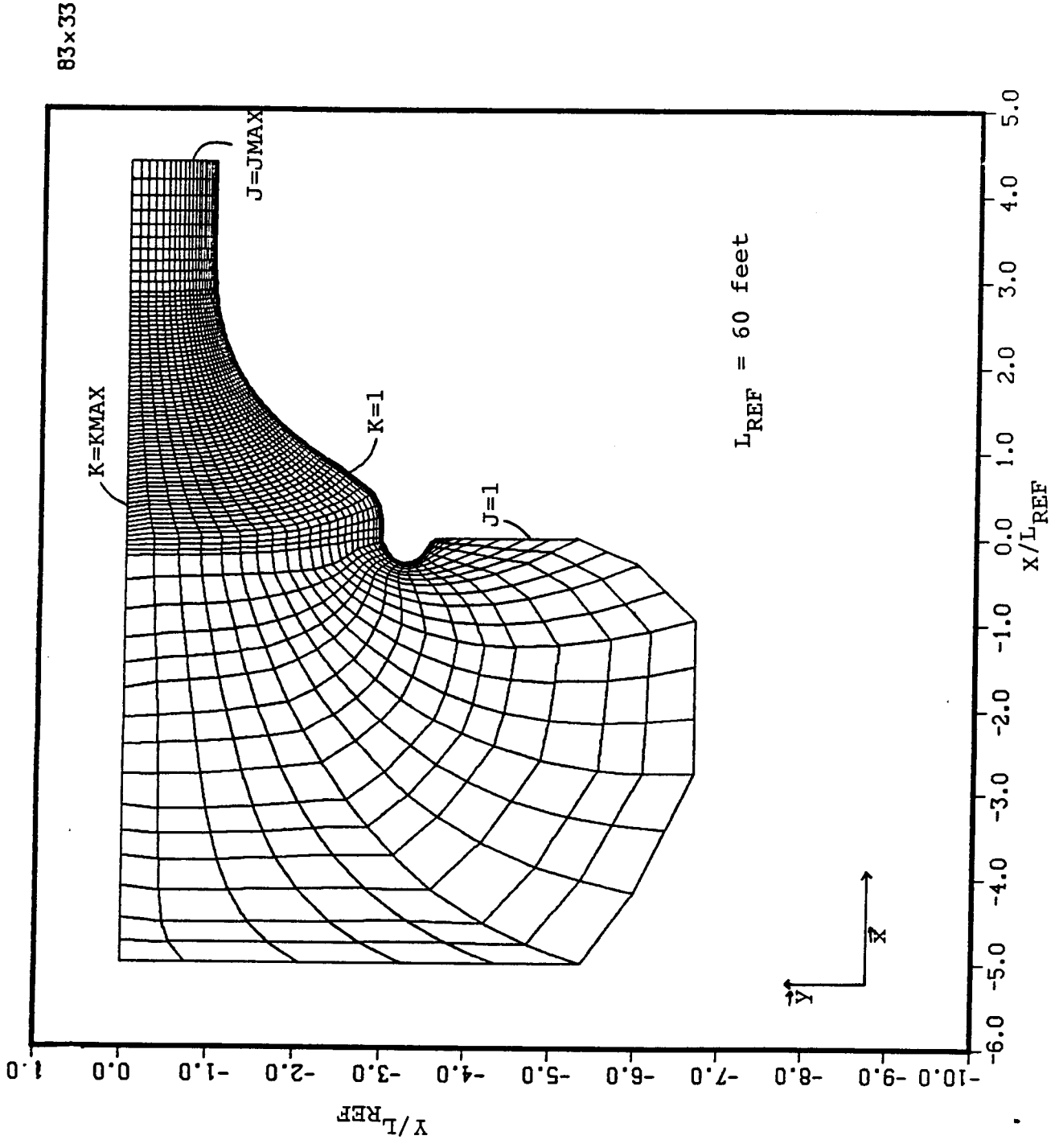

Figure 7. Planar grid in the z-plane, L = 1 - turbulent cases.

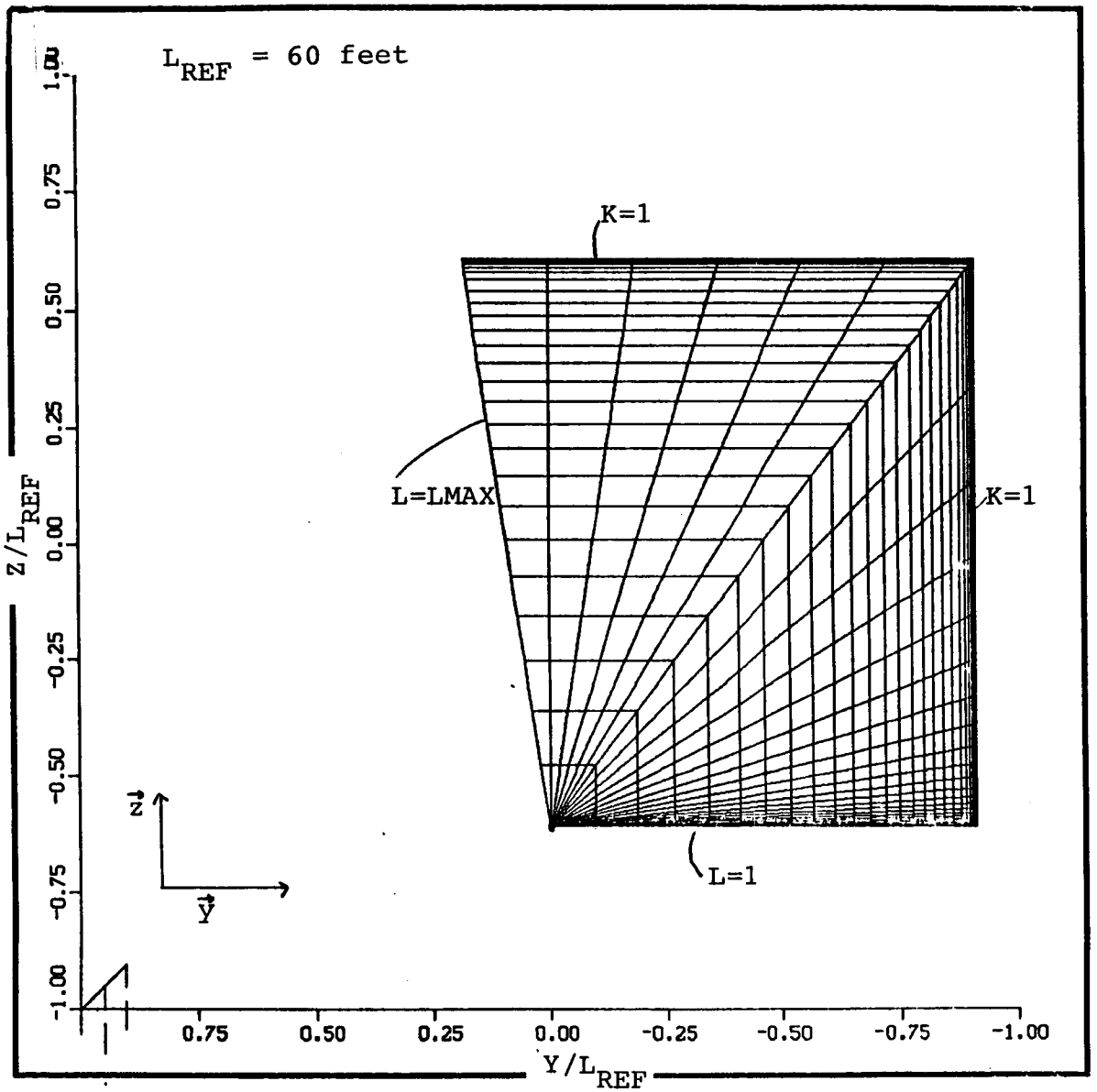

Figure 8. Cross-section plane grid, x = 210 feet - turbulent cases.

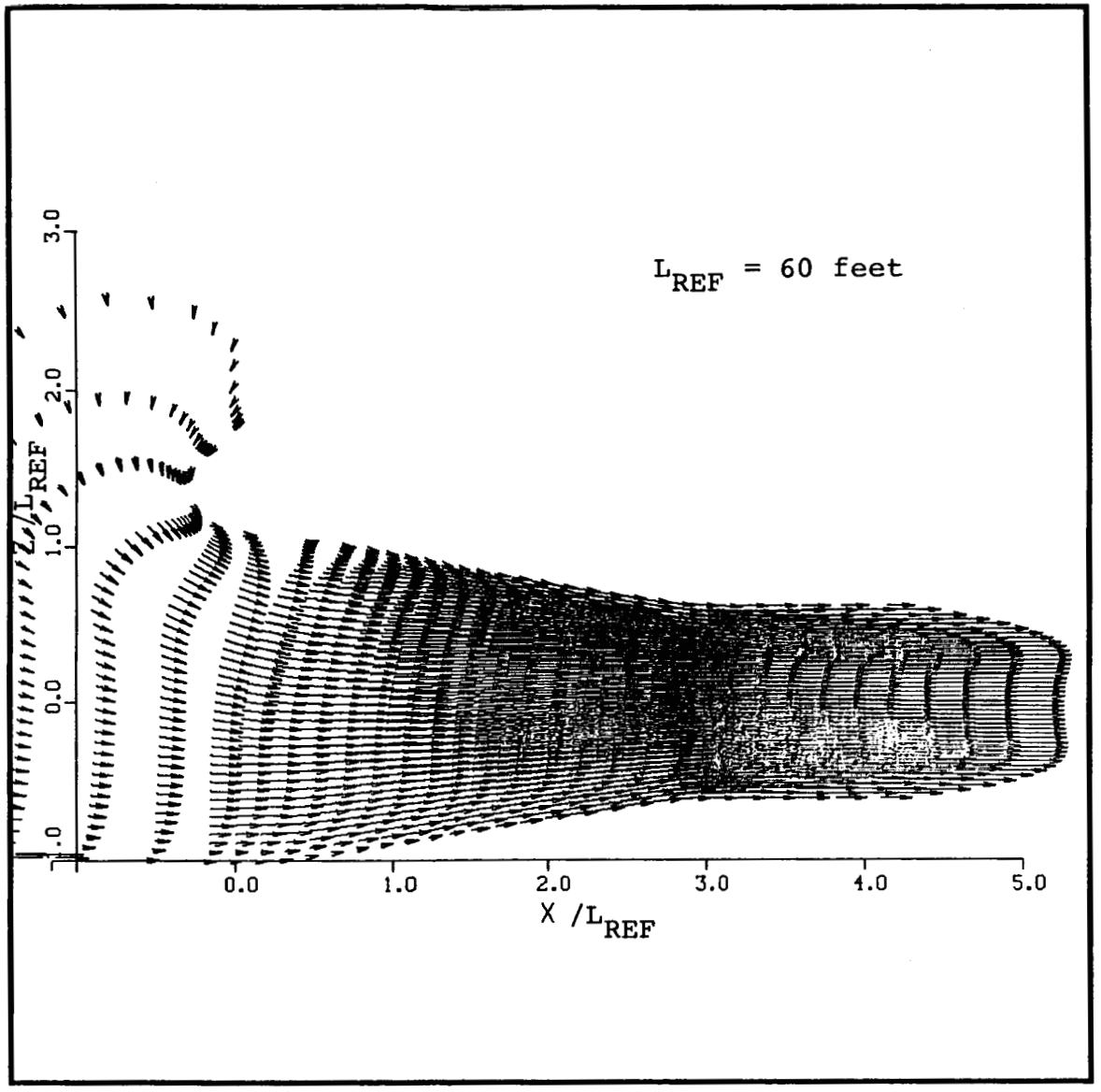

Figure 9. Velocity vectors in the plane L =16.

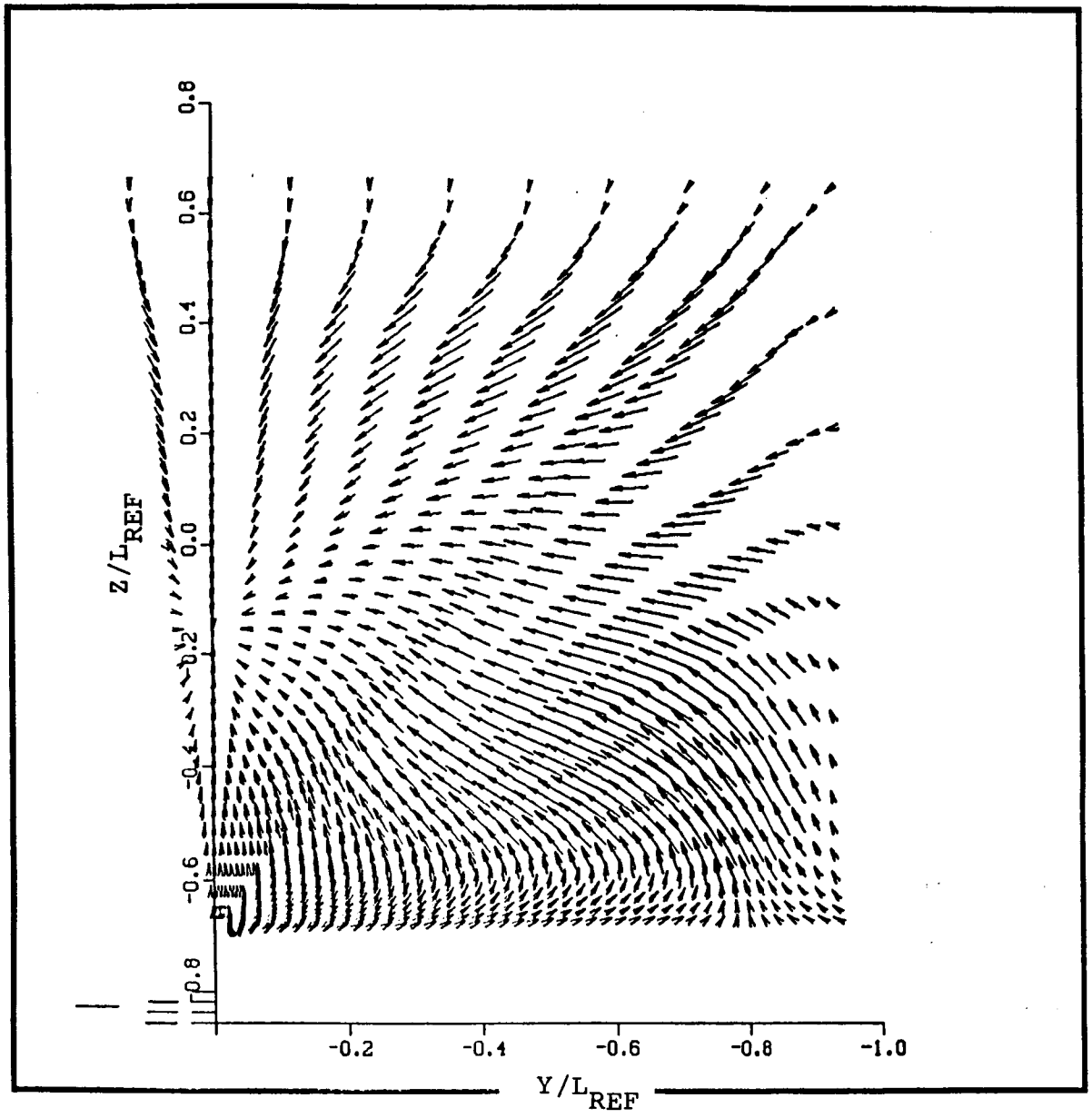

Figure 10. Velocity vectors in the cross-section plane, x= 210 feet.

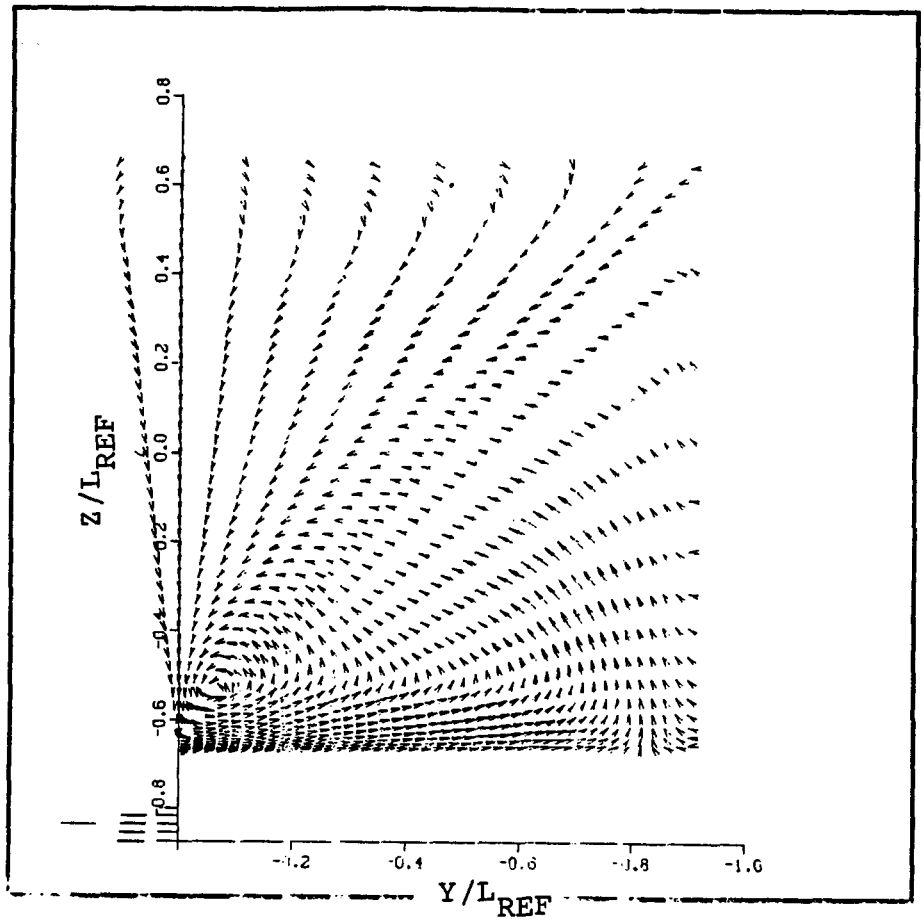

Figure 11. Velocity vectors in the cross-section plane, x = 240 feet.

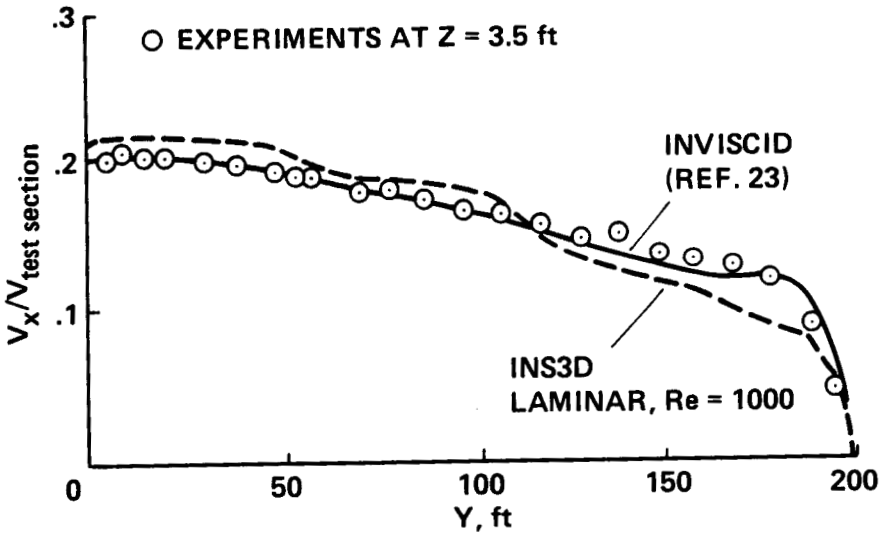

12. Normalized axial velocity variation with the spanwise distance y at x = -27 feet.

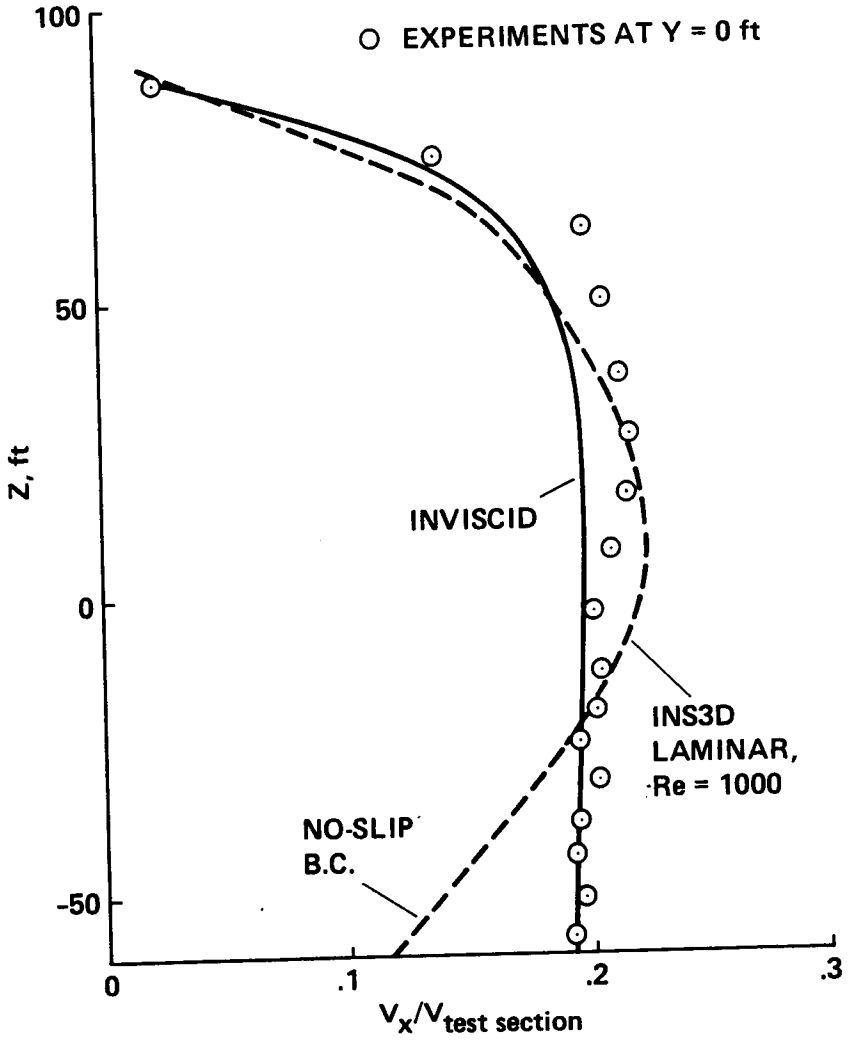

13. Normalized axial velocity variation with height z, at x = -27 feet.

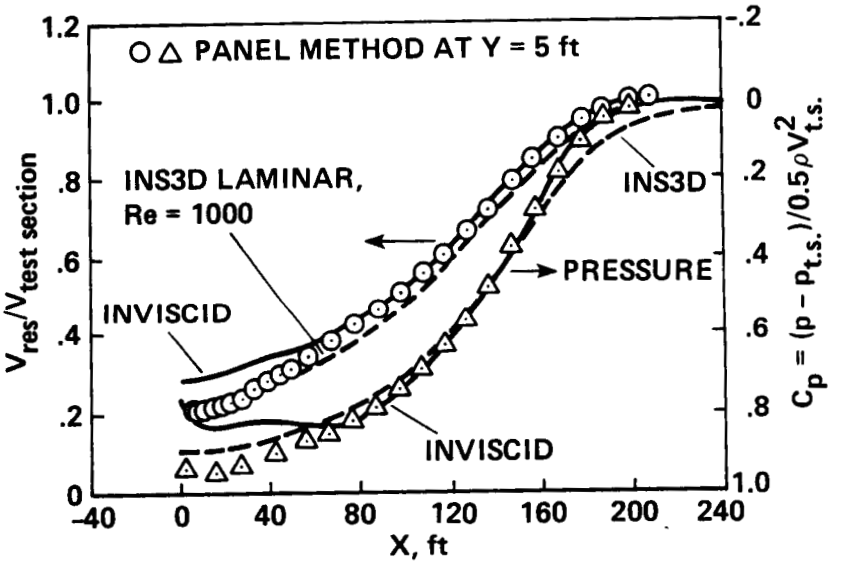

14. Centerline velocity (resultant) and tunnel floor centerline pressure variation with the downstream distance.

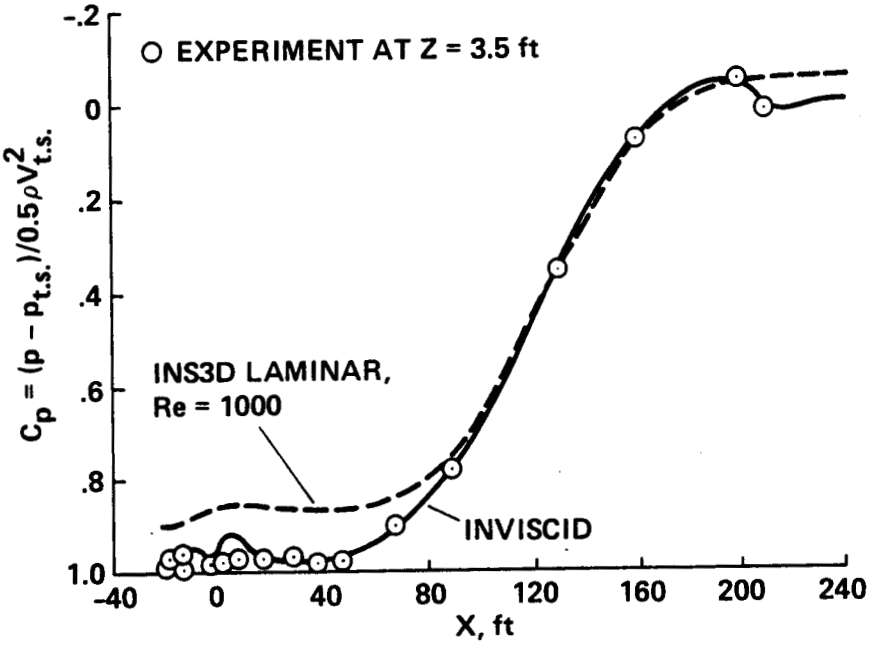

15. Pressure variation on the side wall centerline with the downstream distance x.

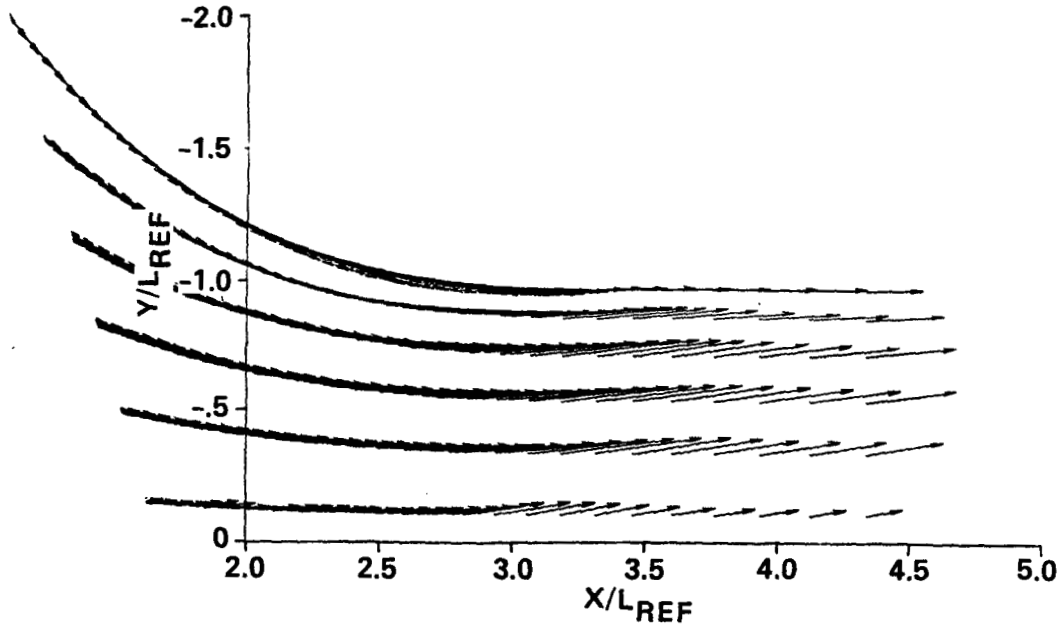

16 a. Velocity vectors in the plane L = 3.

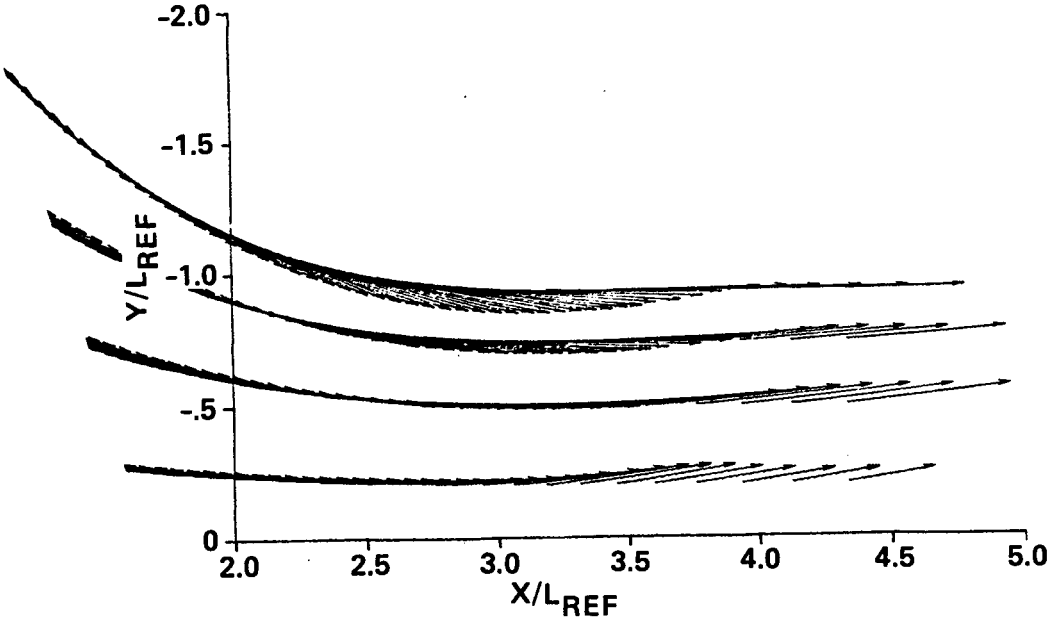

16 b. Velocity vectors in the plane L = 5.

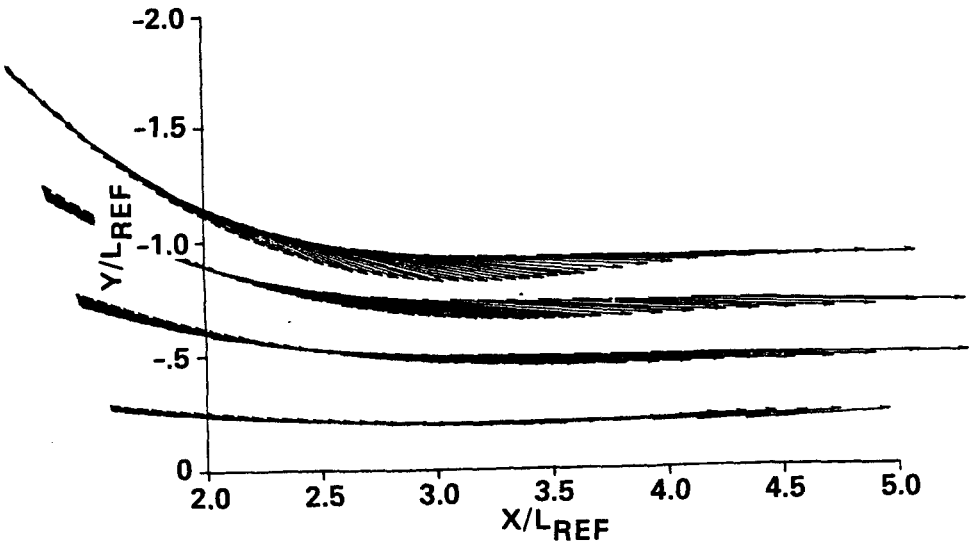

16 c. Velocity vectors in the plane L = 10.

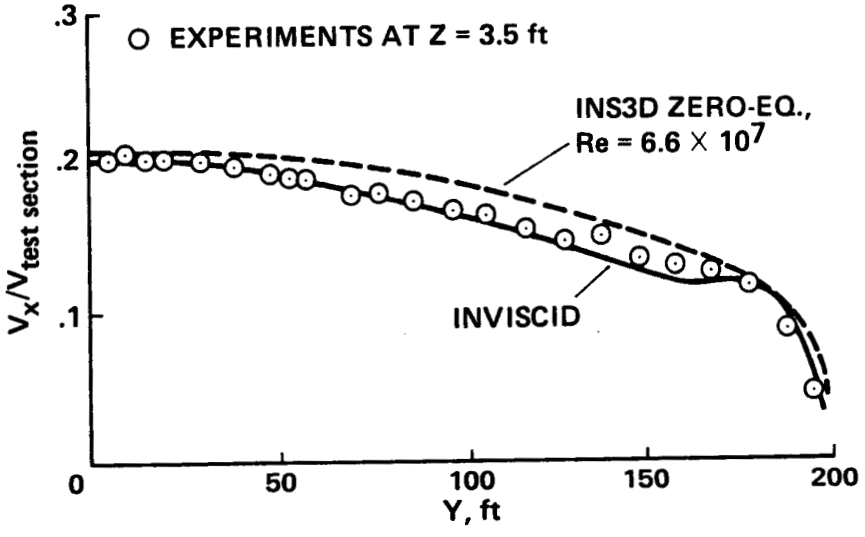

17. Normalized axial velocity variation with the spanwise distance at x = -27 feet, zero-equation model.

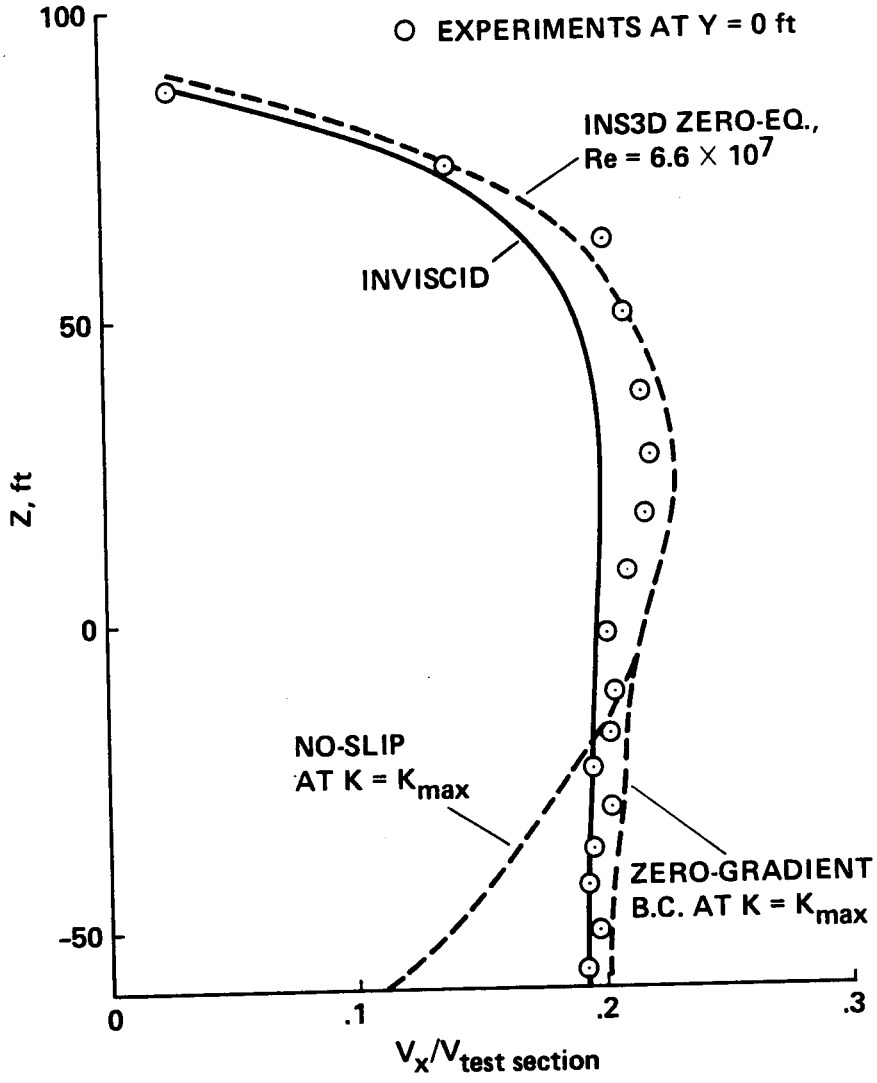

18. Normalized axial velocity variation with height z at x = 27 feet, zero-equation model.

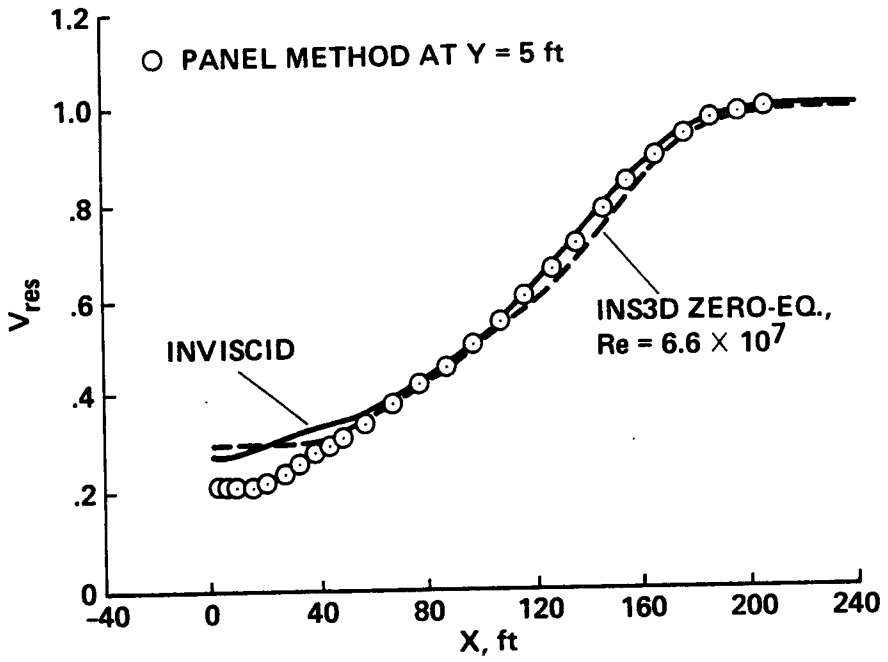

19. Velocity resultant variation with the downstream distance, zero-equation model.

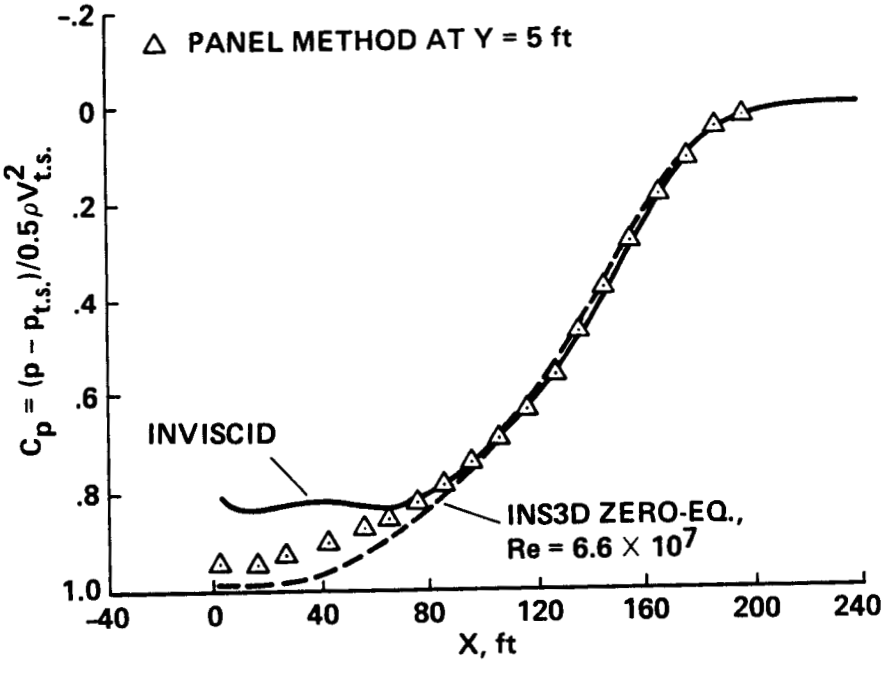

20. Tunnel floor centerline pressure variation with the downstream distance, zero-equation model.

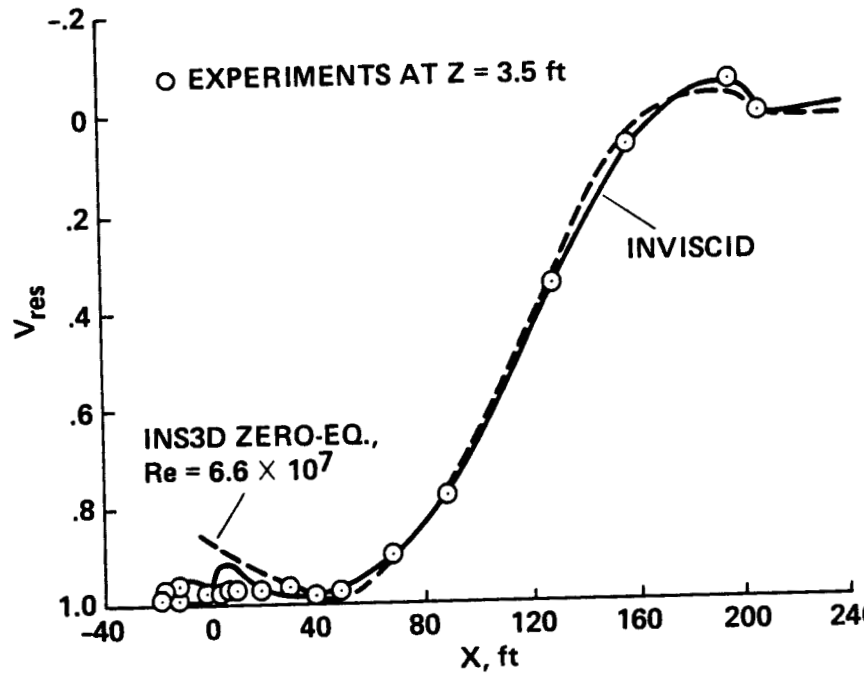

21. Pressure variation on the side wall centerline with the downstream distance x, zero-equation model.

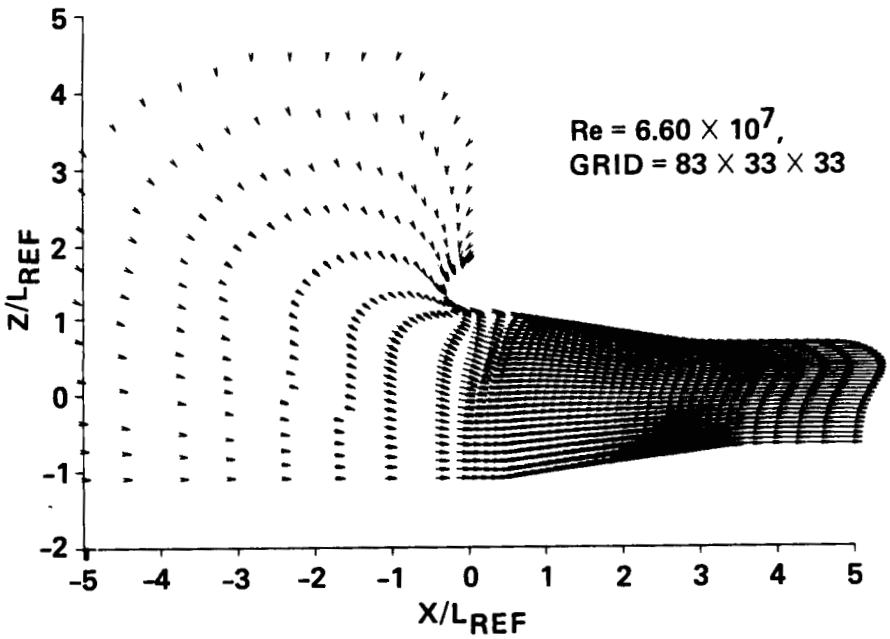

22. Velocity vectors in the plane L = 22, zero-equation model.

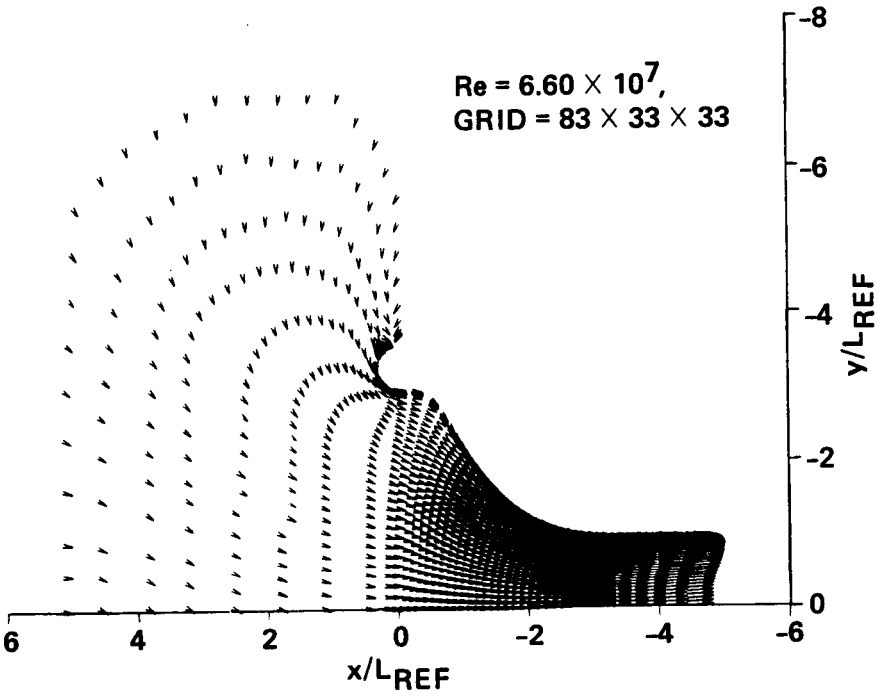

23. Velocity vectors in the plane L = 15, zero-equation model.

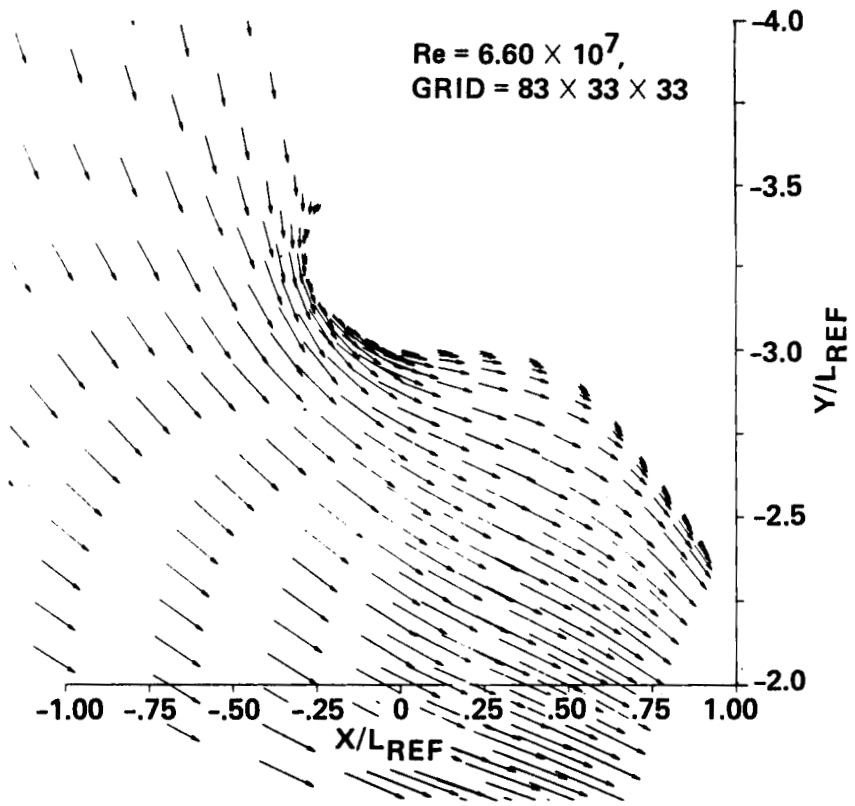

24. Enlarged velocity vectors plot in the plane L = 15 near the inlet cowl, zero-equation model.

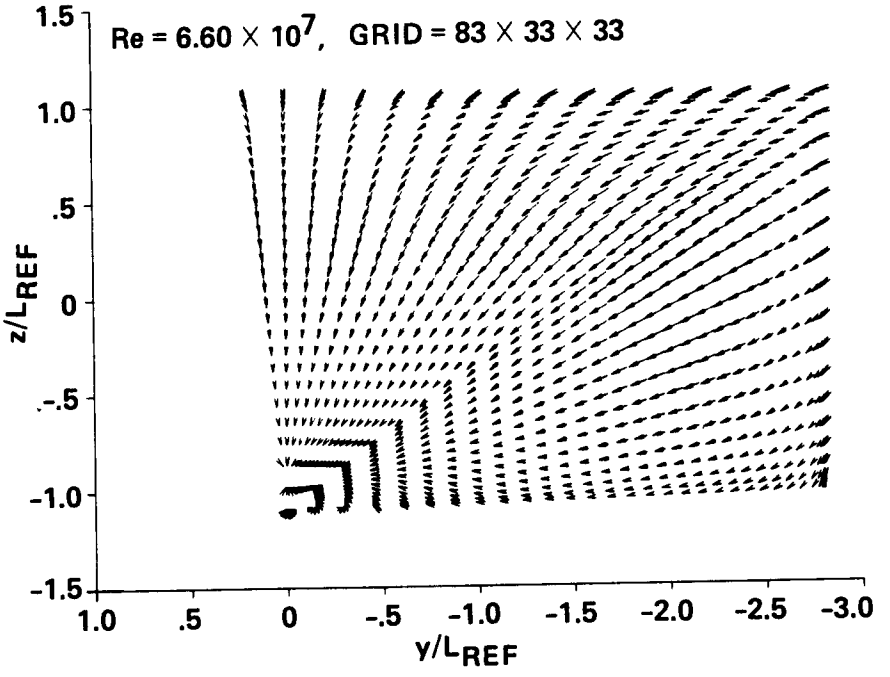

25 a. Crossflow velocity vectors at x = 32 ft, zero-equation model.

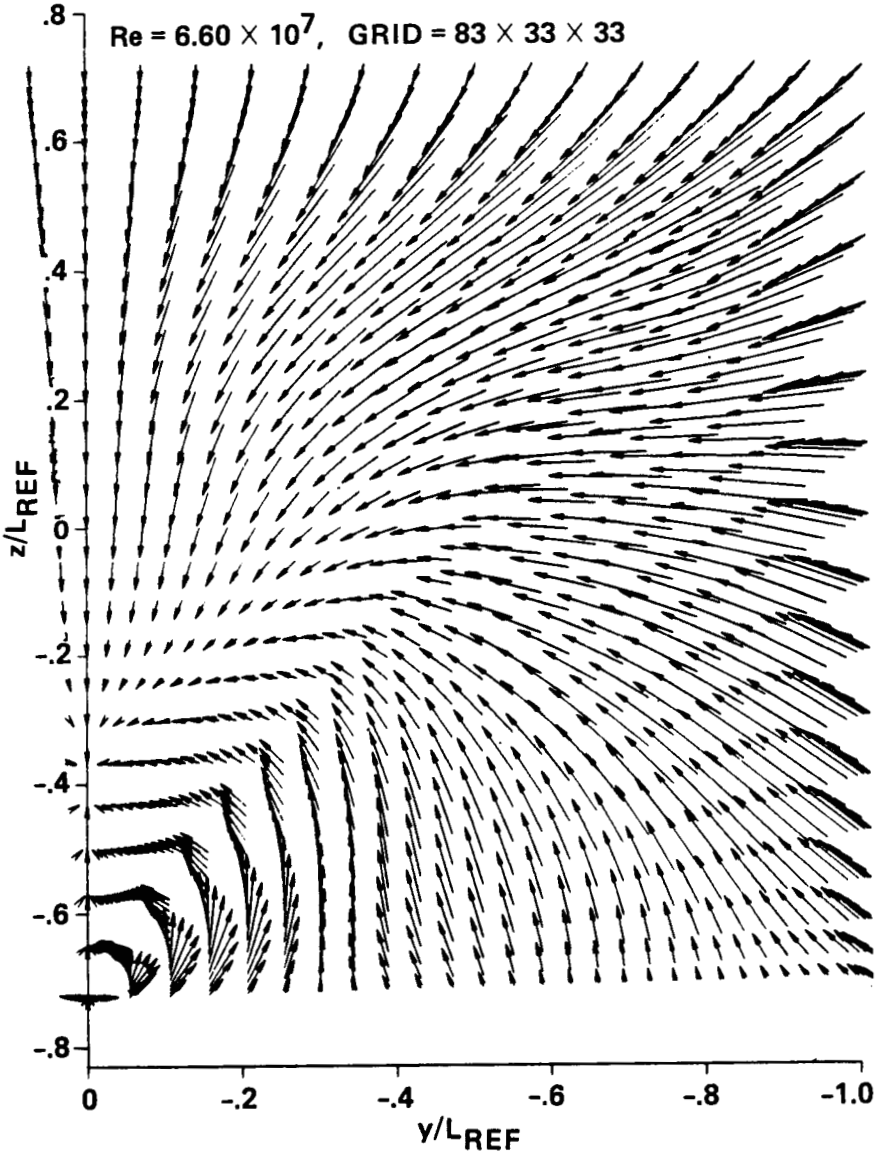

25 b. Crossflow velocity vectors at x = 164 ft, zero-equation model.

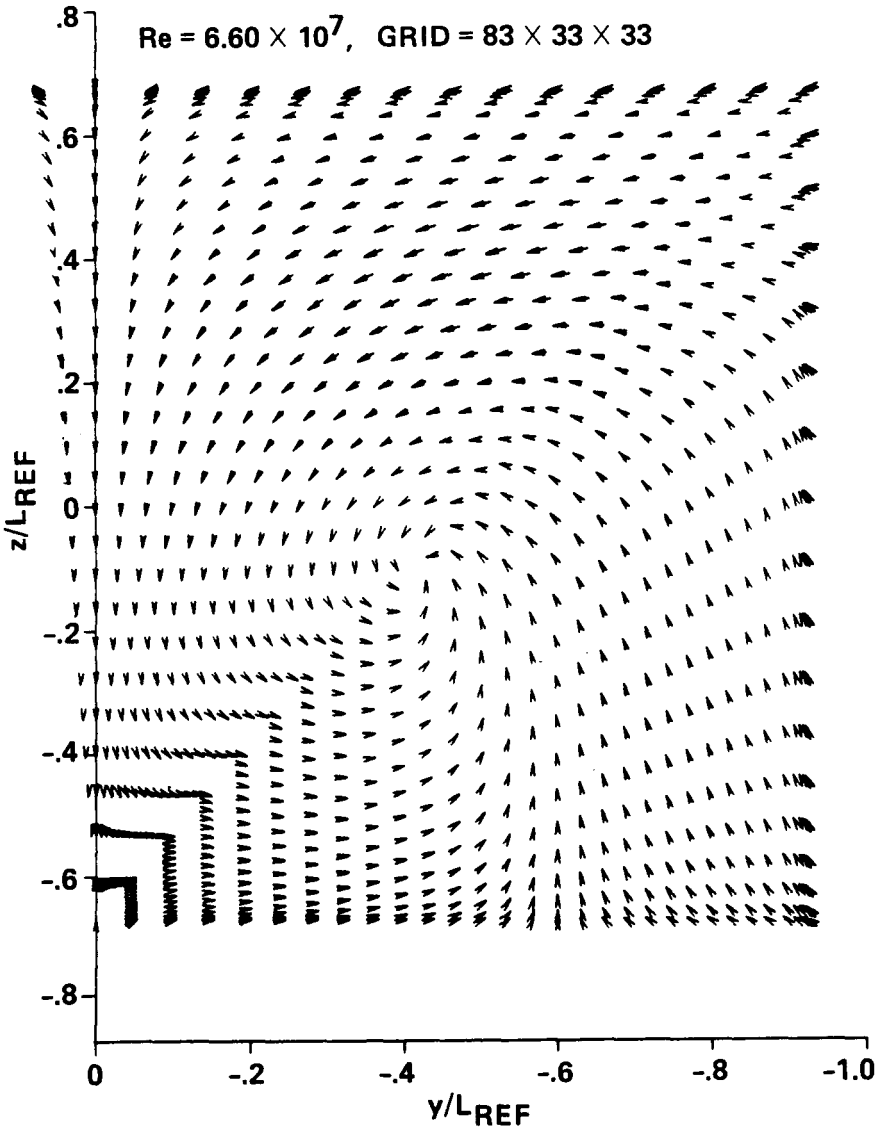

25 c. Crossflow velocity vectors at x = 228 ft, zero-equation model.

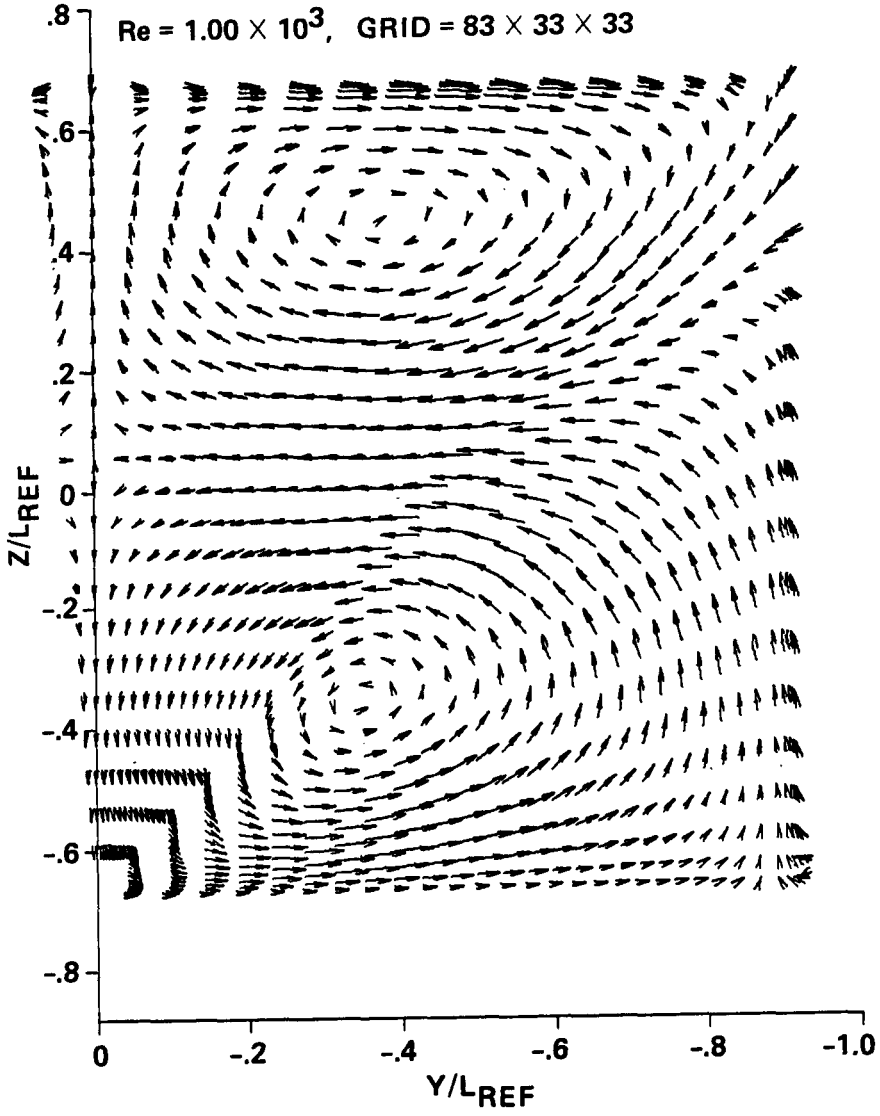

26. Crossflow velocity vectors at x = 228 ft using no-slip boundary conditions at K = KMAX.

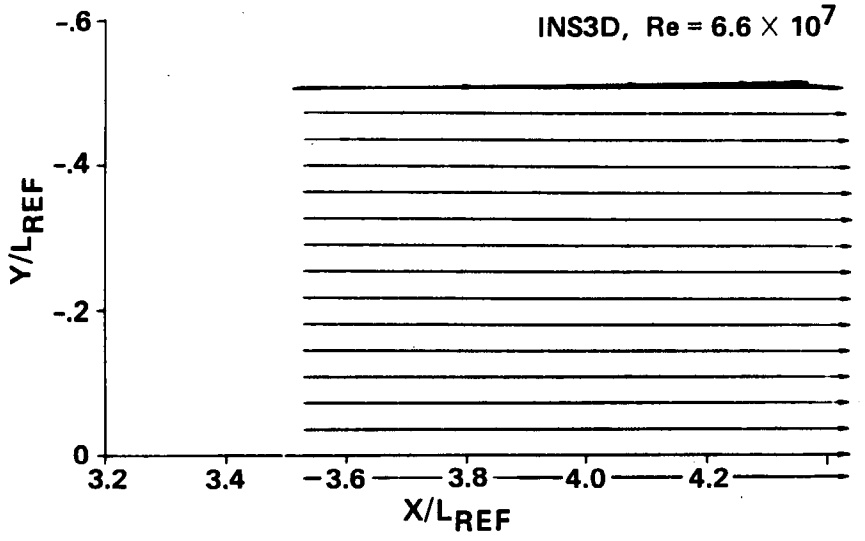

27. Velocity vectors at x = 210 ft along K = 22.

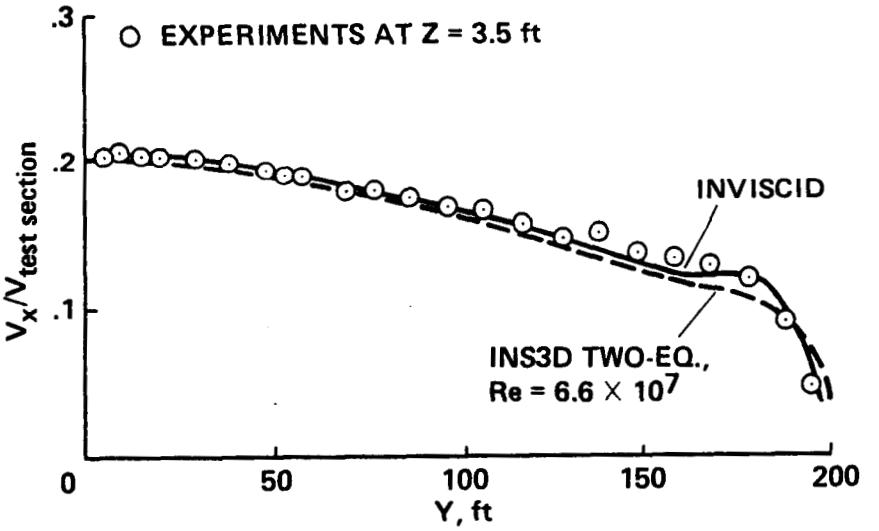

28. Normalized axial velocity variation with the spanwise distance y, two-equation model.

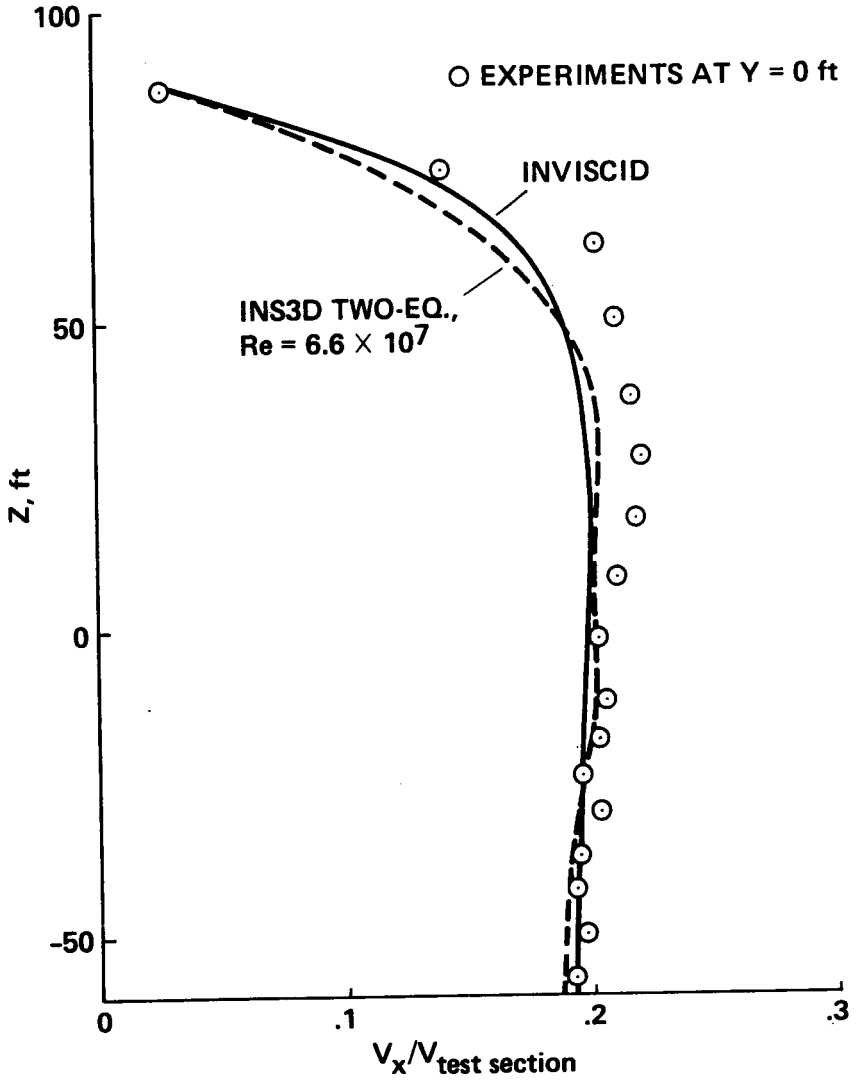

29. Normalized axial velocity variation with height z, two-equation model.

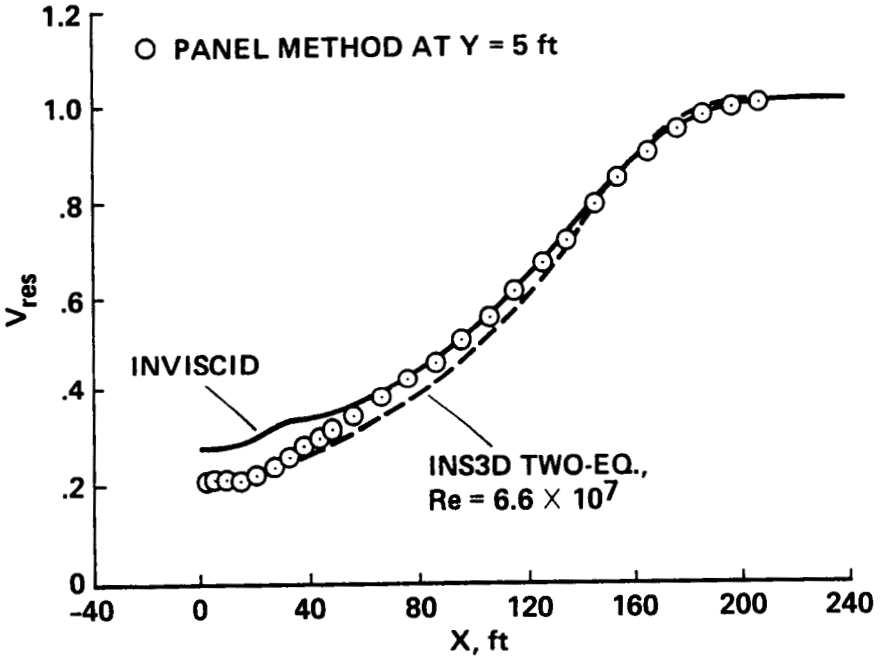

30. Velocity resultant variation with the downstream distance, two-equation model.

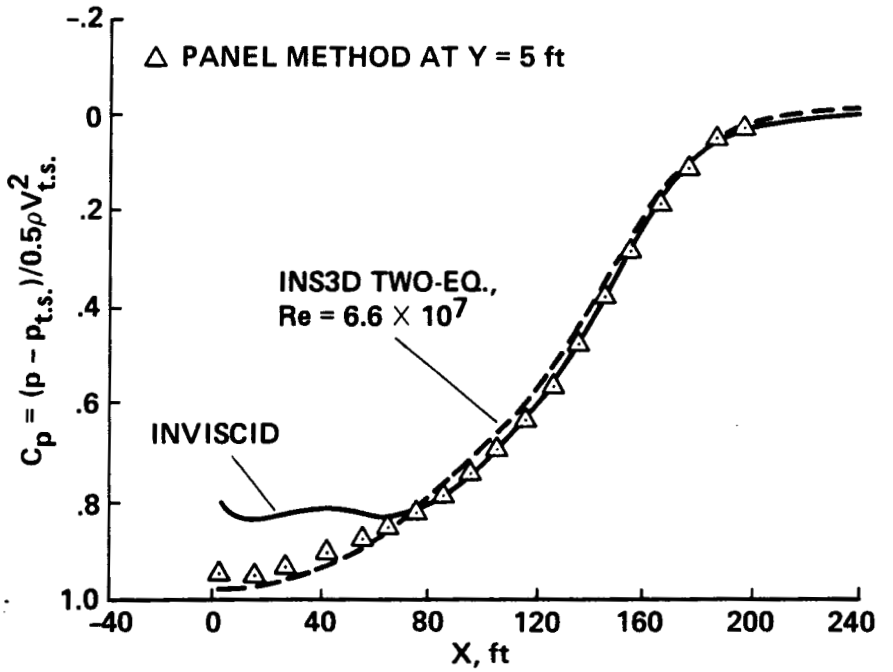

31. Tunnel floor centerline pressure variation with the downstream distance, two-equation model.

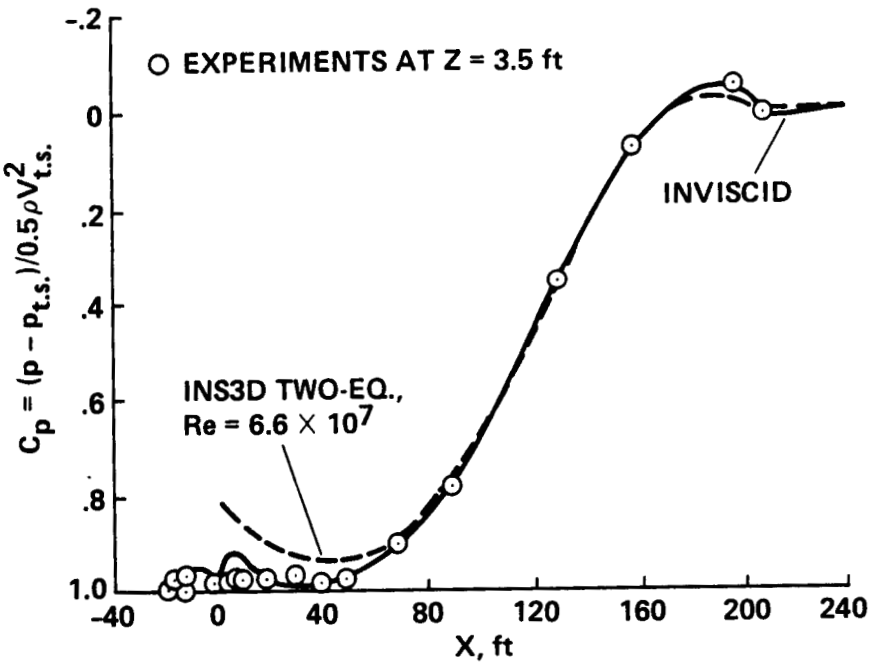

32. Pressure variation on the side wall centerline with the downstream distance x, two-equation model.

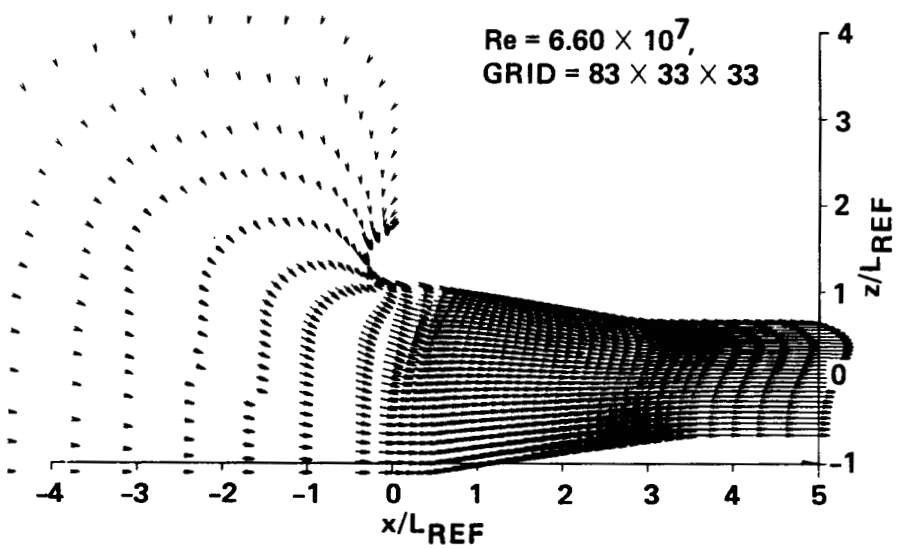

33. Velocity vectors in the plane L = 22, two-equation model.

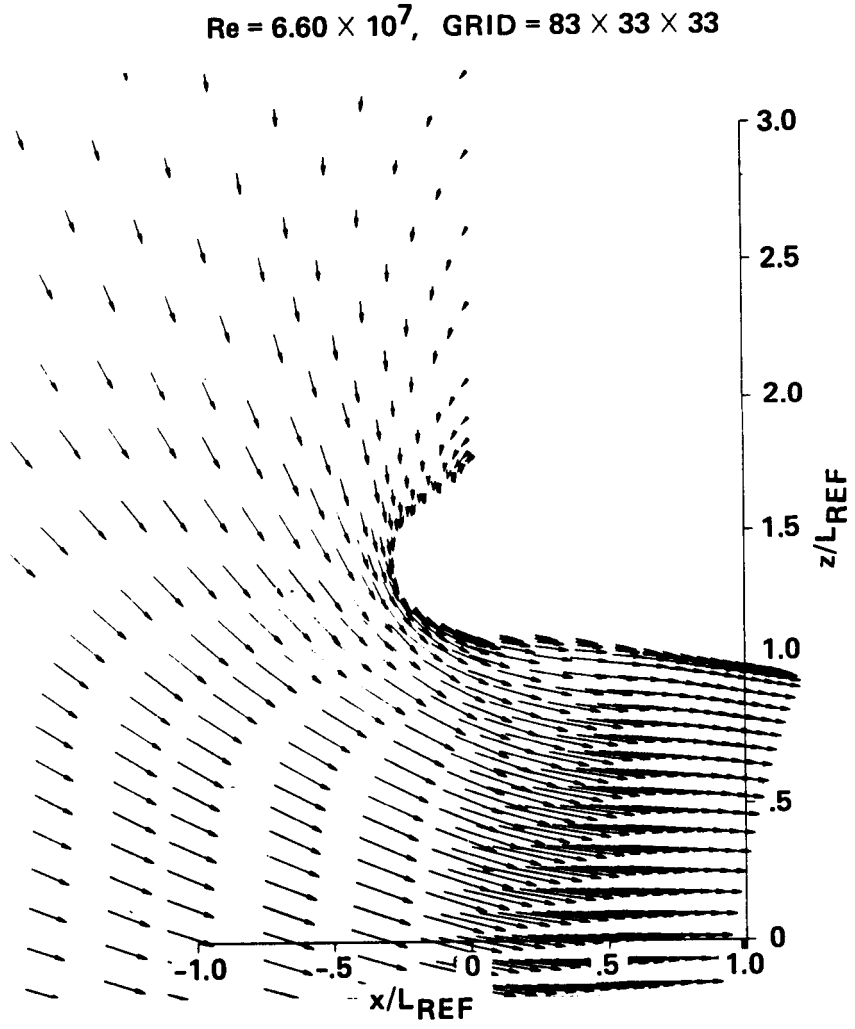

34. Enlarged velocity vectors in the plane L = 22 near the inlet cowl, two-equation model.

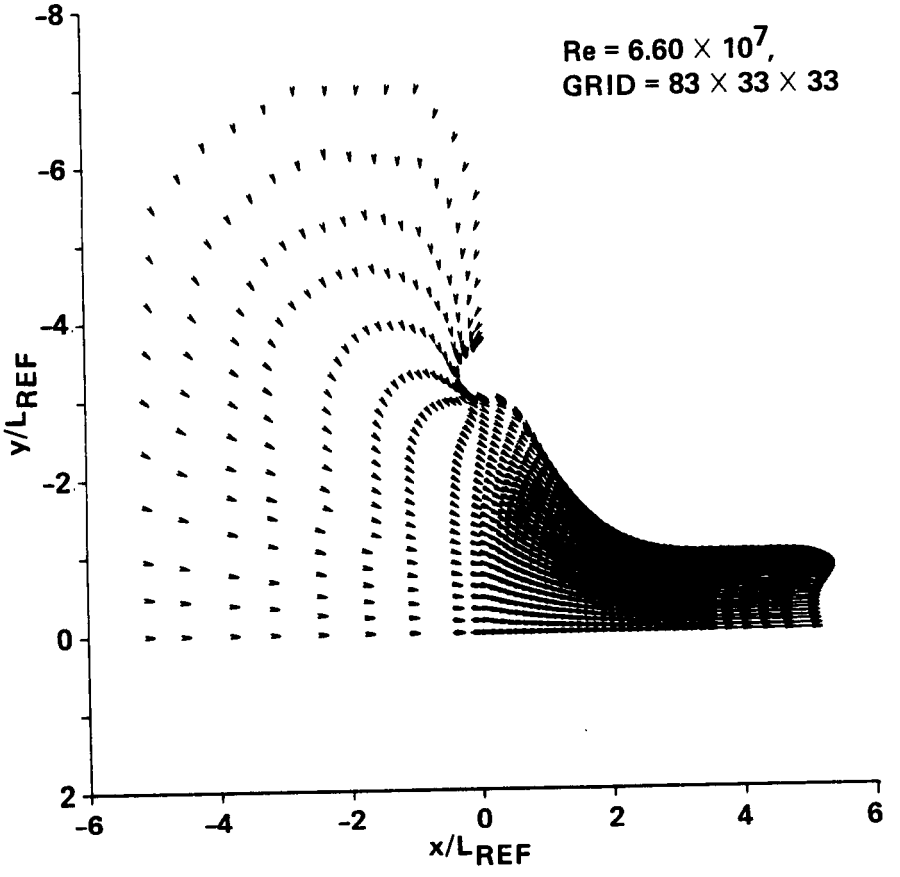

35. Velocity vectors in the plane L = 15, two-equation model.

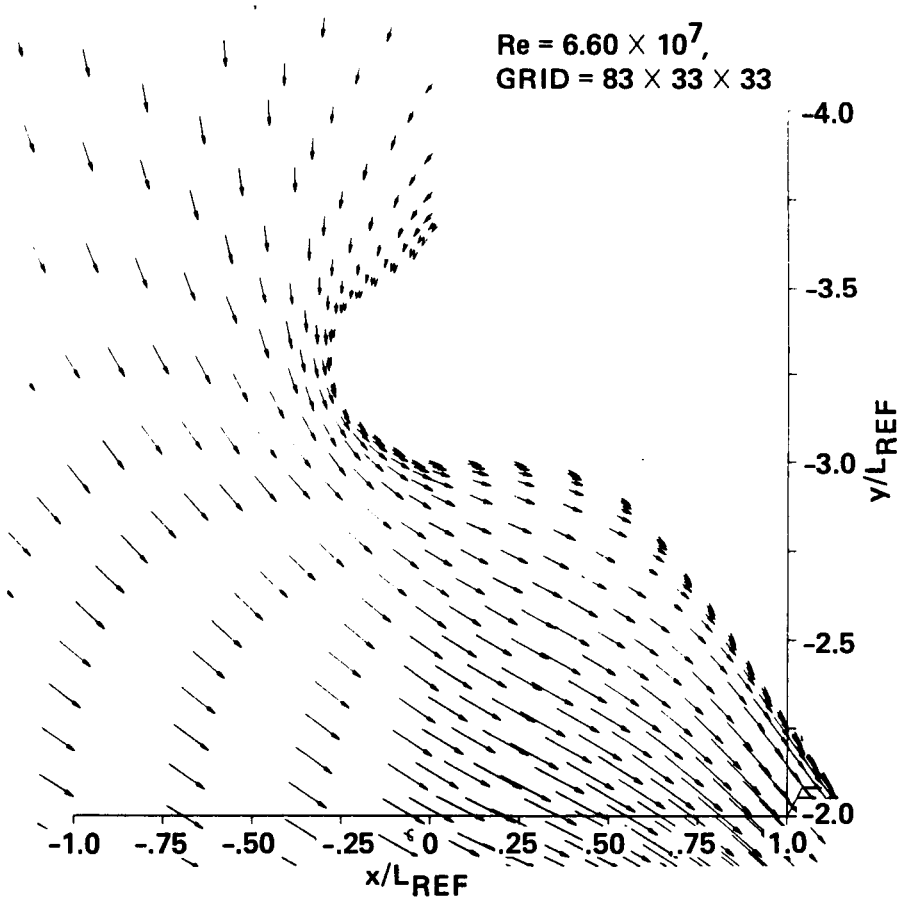

36. Enlarged velocity vectors in the plane L = 15 near the inlet cowl, two-equation model.

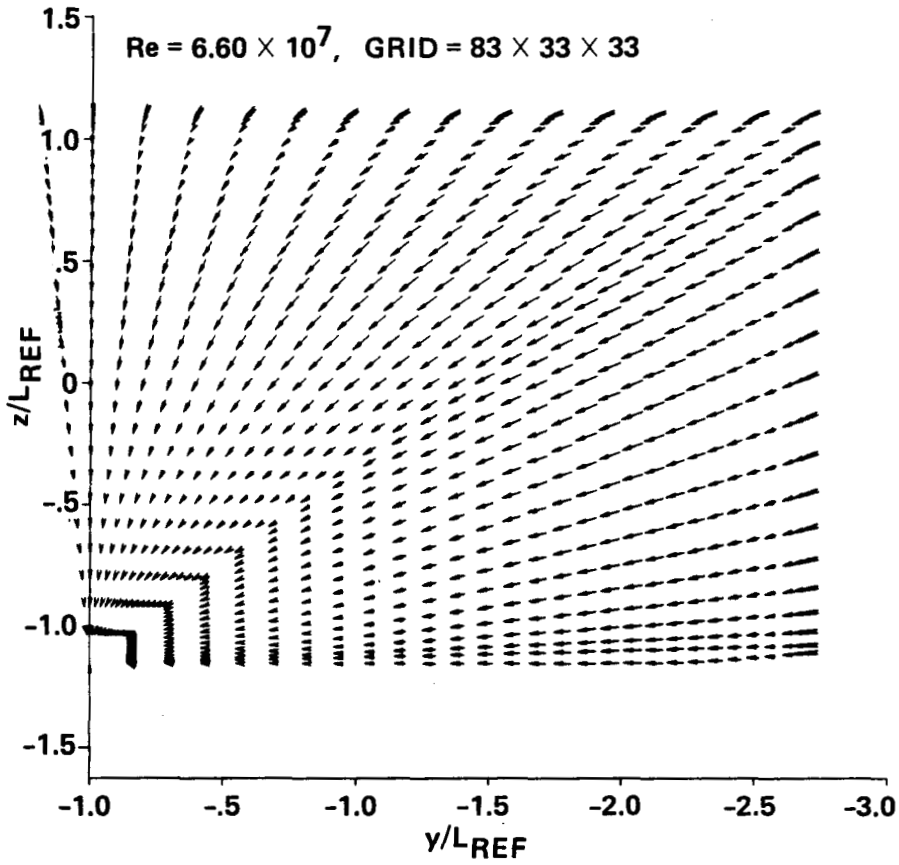

37 a. Crossflow velocity vectors at x = 32 ft, two-equation model.

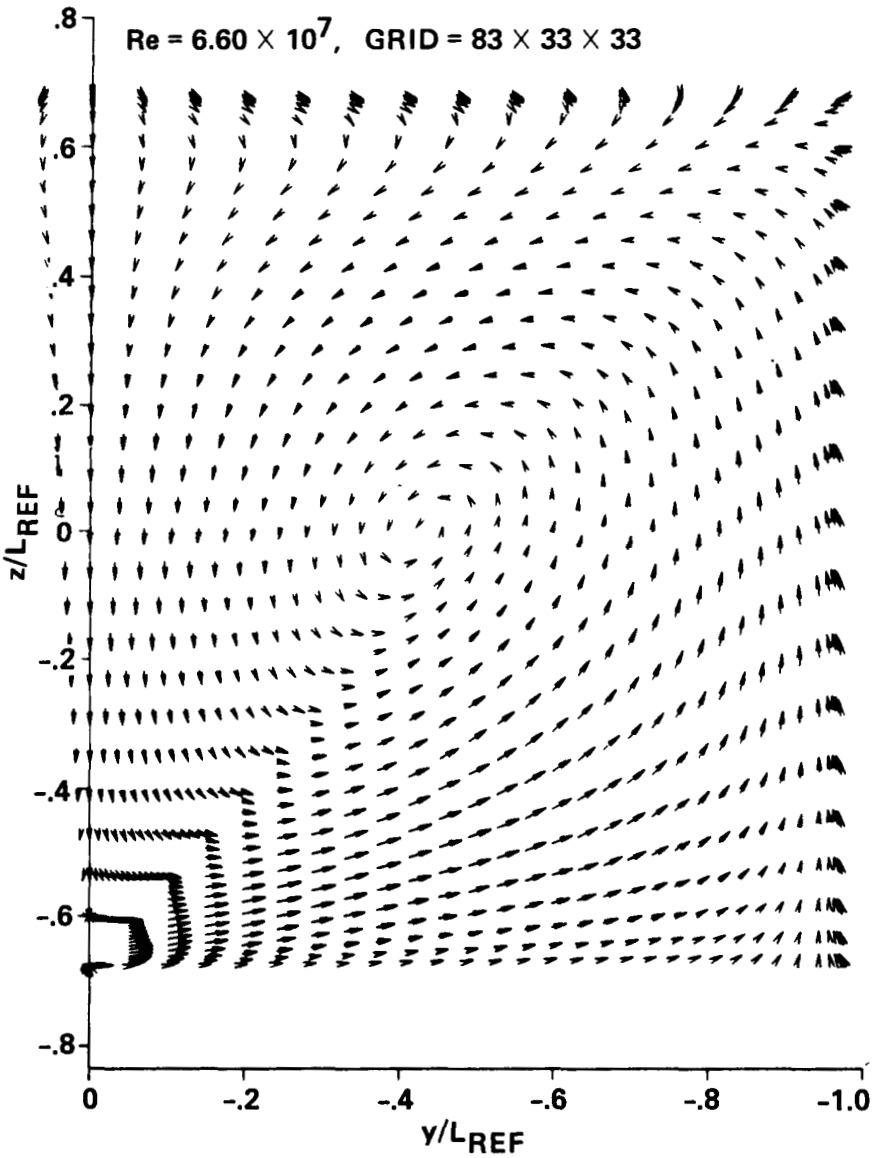

37 b. Crossflow velocity vectors at x = 228 ft, two-equation model.

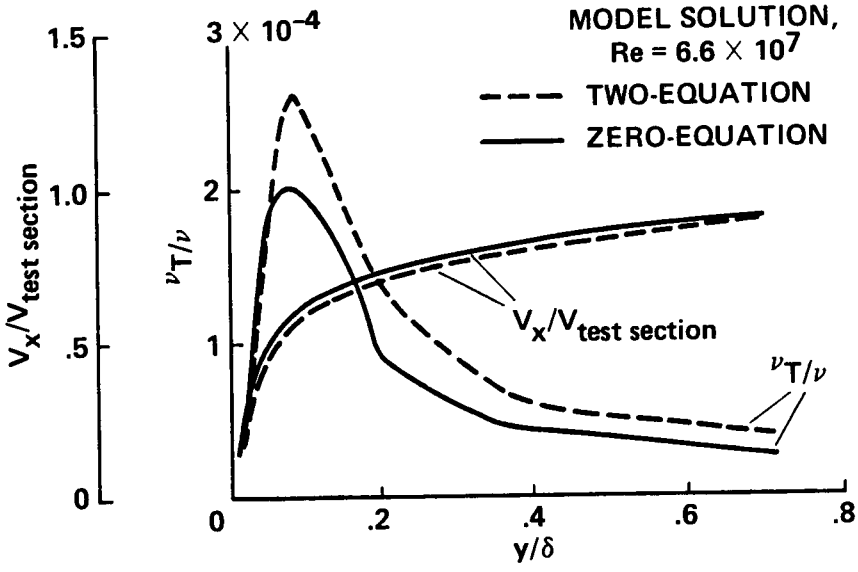

38. Comparisons of eddy viscosities and velocity profiles for the zero- and two-equation models.

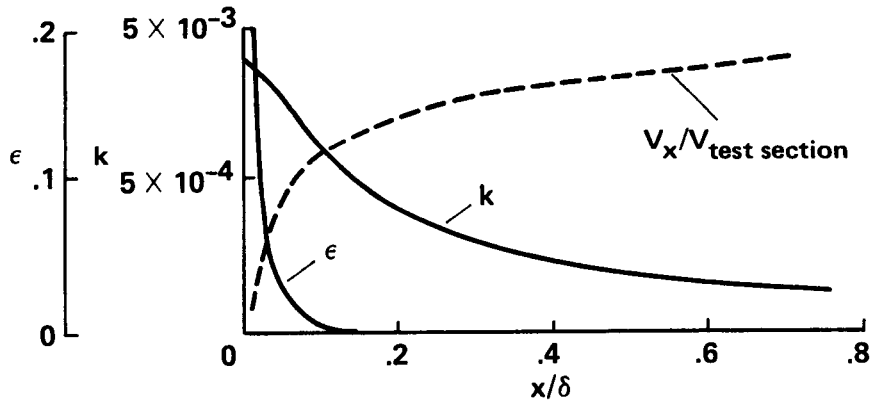

39. Turbulent kinetic energy and dissipation rate of turbulent kinetic energy at x = 210 ft along L=22.

1. Report No.	2. Government Accession No.	3. Recipient's Catalog No
177431		

4. Title and Subtitle	5. Report Date
INCOMPRESSIBLE VISCOUS FLOW SIMULATIONS OF THE NFAC WIND TUNNEL	June 1986
	6. Performing Organization Code
7. Author(s)	8. Performing Organization Report No
Joelle Milene Champney	ATM-FR-25-012
	10. Work Unit No.
9. Performing Organization Name and Address	11. Contract or Grant No.
Applied & Theoretical Mechanics, Inc. 4501 Sequoyah Road Oakland, California 94605	NAS2-12187
	13. Type of Report and Period Covered
12. Sponsoring Agency Name and Address	Final Report for June 85 - June 86
National Aeronautics and Space Administration Washington, DC 20546	14. Sponsoring Agency Code
	507-05-01

15. Supplementary Notes

Point of Contact: Dochan Kwak, Ames Research Center, M/S 202-14
Moffett Field, CA 94035 (415) 694-6743
or FTS 464-6743

16. Abstract

The capabilities of an existing three-dimensional incompressible Navier-Stokes flow solver, INS3D, are extended and improved to solve turbulent flows through the incorporation of zero- and two-equation turbulence models. The two-equation model equations are solved in their high Reynolds number form and utilize wall functions in the treatment of solid wall boundary conditions. The implicit approximate factorization scheme is modified to improve the stability of the two-equation solver. Applications to the three-dimensional viscous flow inside the 80 by 120 feet open return wind tunnel of the National Full Scale Aerodynamics Complex (NFAC) are discussed and described.

17. Key Words (Suggested by Author(s))	18. Distribution Statement
Incompressible Turbulent Implicit Wall function Navier-Stokes	Unclassified - Unlimited Subject Category - 02

19. Security Classif. (of this report)	20. Security Classif. (of this page)	21. No. of Pages	22. Price*
Unclassified	Unclassified	87	

*For sale by the National Technical Information Service, Springfield, Virginia 22161